https://doi.org/10.5194/egusphere-2026-4336
Preprint. Discussion started: 18 August 2026

A monthly-climatological parameterization of the surface leading-crestline morphology for internal solitary waves in the northeastern South China Sea

Yanze Yin[1,2], Yankun Gong[3], and Xu Wang[1,2]

[1] Key Laboratory for Mechanics in Fluid Solid Coupling Systems, Institute of Mechanics, Chinese Academy of Sciences, Beijing 100190, China
[2] School of Engineering Science, University of Chinese Academy of Sciences, Beijing 100049, China
[3] State Key Laboratory of Tropical Oceanography, South China Sea Institute of Oceanology, Chinese Academy of Sciences, Guangzhou 510301, China

Correspondence: Xu Wang (wangxu@imech.ac.cn)

Abstract. Internal solitary waves (ISWs) in the northern South China Sea are among the most energetic worldwide, and ISWs can cause severe impacts on offshore platforms and underwater operations; rapid forecasting of the propagation process of ISWs is therefore a practical need in ocean engineering. In the actual ocean, the leading-crestline morphology at the ocean surface often provides a general indication of the propagation and evolution of the underlying internal wave. This study develops a parametric representation of surface-expressed leading-crestline morphology for the east-of-Dongsha segment of the Luzon Strait–Dongsha corridor. Specifically, leading crestlines are extracted from sea-surface-height-gradient (SSHG) fields of nonhydrostatic MITgcm simulations forced by World Ocean Atlas 2018 monthly stratification, using Canny edge detection and density-based clustering. The analysis results indicate that, under the assumption of monthly climatological stratification, the crestlines binned by their along-corridor location cluster around a common, location-dependent propagation morphology that is represented by cubic polynomial curves and summarized in monthly coefficient tables. Evaluated against independent satellite-derived crestlines, the representative curves achieve a mean root-mean-square error (RMSE) of approximately 0.01° in longitude and a mean R^2 of 0.870. Consequently, by analyzing the monthly average climate-state leading-crestline morphology across different months of the year, we can identify the key characteristics of internal wave propagation in the northeastern South China Sea.

Keywords: Internal solitary waves; South China Sea; monthly-climatological leading-crestline morphology

1 Introduction

Internal solitary waves (ISWs) are large-amplitude, nonlinear submesoscale disturbances that propagate along oceanic pycnoclines and serve as a primary mechanism for cross-shelf energy cascade, turbulent diapycnal mixing, and momentum transfer between the deep ocean and continental margins (Apel et al., 1985; Alford et al., 2015). The northern South China Sea (NSCS) is widely recognized as one of the most energetic regions for ISW activity worldwide (Alford et al., 2015; Bai et al.,

https://doi.org/10.5194/egusphere-2026-4336
Preprint. Discussion started: 18 August 2026

2014, 2017; Cai et al., 2012; Guo and Chen, 2014; Liu and Hsu, 2004; Liang et al., 2019; Ramp et al., 2022). Powerful internal tides generated at the Luzon Strait evolve into westward-propagating solitary wave packets across the deep basin (Simmons et al., 2011; Cai et al., 2002; Ramp et al., 2004; Zhao and Alford, 2006; K. Zeng et al., 2024). Leading solitary waves can attain isopycnal displacements exceeding 170 m and drive near-surface currents of up to 3m s^{-1}, producing intense vertical shear and elevated diapycnal mixing across the pycnocline (Li, 2005; Jiang et al., 2025; Xun et al., 2025). The variable intrusion of the Kuroshio through the Luzon Strait and the associated mesoscale eddy field further deflect internal tidal beams and modulate downstream ISW characteristics in ways that remain difficult to predict (Huang et al., 2024; Gong et al., 2025). Consequently, the high energy and strong vertical shear associated with these waves can impose substantial hydrodynamic loading on offshore installations, with implications for marine risers, deep-water platforms, and underwater vehicle operations (Li, 2005; Jiang et al., 2025). Reliable and rapid ISW prediction has therefore become a practical necessity in physical oceanography and ocean engineering. Although ISWs are subsurface waves, their propagation is directly imprinted on the sea surface: the convergent and divergent currents induced above the wave troughs modulate short surface waves, so that the leading wave of each ISW packet manifests in optical and SAR imagery as a surface-expressed leading crestline (Fu and Holt, 1982; Liang et al., 2019). This crestline is the sea-surface expression of the underlying internal wave—its position locates the surface signature of the leading wave, its local normal (oriented by the predominantly westward propagation in this region) indicates the local propagation direction, and its along-crest curvature reflects the accumulated effects of spatially differential propagation, including refraction—and it therefore constitutes a directly observable descriptor of ISW propagation and evolution (Zhang et al., 2019; Zhang and Li, 2024).

Accurate prediction of ISW crestline propagation and morphological evolution is central to both physical understanding and operational forecasting, because crestline geometry directly constrains wave arrival time, propagation pathway, and spatial footprint. Existing approaches include nonhydrostatic numerical models, satellite observations, and data-driven methods. High-resolution models such as MITgcm, SUNTANS, and FVCOM can reproduce ISW generation and propagation with good physical fidelity, but basin-scale, nonhydrostatic simulations remain computationally expensive for routine forecasting (Marshall et al., 1997; Fringer et al., 2006; Chen et al., 2006; Min et al., 2023; Gong et al., 2023; Huang et al., 2023, 2024). Satellite SAR and optical imagery provide the most direct two-dimensional view of crestline morphology, yet their value for continuous prediction is constrained by cloud contamination, intermittent revisit sampling, and surface look-alike signatures (Fu and Holt, 1982; Li, 2005; Liang et al., 2019; Kurekin et al., 2020; Dang et al., 2025). Data-driven approaches offer improved computational efficiency, but their skill depends strongly on training samples, and many such methods emphasize scalar propagation metrics rather than the two-dimensional crestline shape itself (Zhang et al., 2021). Taken together, existing approaches have advanced the understanding of ISW propagation from complementary directions. However, a lightweight, physically interpretable, and rapidly evaluable representation of the two-dimensional leading-crestline morphology remains lacking. Such a representation would provide the leading-crestline shape from a precomputed reference and complement event-resolving simulations, intermittent satellite mapping, and training-dependent data-driven models.

https://doi.org/10.5194/egusphere-2026-4336
Preprint. Discussion started: 18 August 2026

A fundamental challenge in predicting the leading-crestline shape is that it results from the combined effects of background circulation, vertical stratification, bathymetric steering, and a range of other environmental and dynamical processes (Xie et al., 2021; Huang et al., 2024). When these factors vary simultaneously in space and time, the resulting crestline deformation, morphological evolution, and nonlinear transformation make it difficult to isolate their respective roles and to obtain a clear and repeatable law governing basin-scale crestline propagation (Cui et al., 2024; Cheng et al., 2024; Sinnett et al., 2022; Ramp et al., 2022). This motivates the adoption of a monthly climatological-mean framework that retains the principal controls on the crestline shape, namely bathymetric steering and the seasonally varying pycnocline structure, while short-term and event-scale perturbations are inherently smoothed by the climatological averaging. Under such a framework, the propagation environment within a given calendar month can be regarded as relatively stable, providing a tractable basis for extracting the large-scale regularity of crestline morphology. Beyond making the propagation environment tractable, this framework also provides the physical basis for characterizing propagation through the surface-expressed crestline alone. It should be emphasized that the leading-crestline morphology extracted in this study is not merely a geometric clustering. This is because, under monthly climatological stratification, the bathymetry is fixed and the monthly-mean stratification prescribes the pycnocline structure, so the horizontal phase-speed distribution—and the associated refraction pattern that bends the wavefront—is set by the month-specific waveguide. Each point on a surface crestline therefore carries more than positional information: the local orientation and curvature record the refraction accumulated as the wave propagates, so that the pycnocline and stratification information is imprinted on the surface geometry. For the present purpose of characterizing the large-scale leading-crestline morphology, the surface expression of the three-dimensional propagation problem can therefore be reduced to a two-dimensional problem for the sea-surface crestline shape, providing the physical foundation for automated image-based analysis of two-dimensional sea surface height gradient (SSHG) fields.

Building on this premise, the present study analyzes SSHG fields derived from nonhydrostatic MITgcm simulations forced by WOA18 monthly-mean stratification (Gong et al., 2023, 2025) and develops a compact parametric representation of the leading-crestline morphology for the east-of-Dongsha segment (117°E–119°E) of the Luzon Strait–Dongsha corridor. The focus is the horizontal surface expression of the leading crestline, including its position, orientation, and curvature; event-specific waveform, amplitude, vertical displacement, and other subsurface structures require a separate three-dimensional treatment and are reserved for subsequent work. Specifically, this study first extracts leading crestlines from the SSHG fields through an automated image-processing workflow combining Canny edge detection with density-based unsupervised clustering. The extracted crestlines are then aggregated by calendar month and by their along-corridor location (Section 2.5), and the crestlines in each group are used to construct representative curves described by location-dependent cubic polynomials, yielding a coefficient table for each month; the August table is presented here. Finally, the resulting representative curves are evaluated against independent satellite-derived crestlines from the IOCAS 22-year internal-wave dataset (Zhang and Li, 2024), with August as the primary demonstration. Because the workflow yields coefficient tables for all twelve calendar months, the evaluation is not confined to August: individual cases from May, June, and July are further examined against their month-matched representative curves as illustrative examples, providing preliminary case-level evidence that the monthly tables

https://doi.org/10.5194/egusphere-2026-4336
Preprint. Discussion started: 18 August 2026

remain applicable beyond August. Throughout, the MITgcm-derived SSHG fields are used to construct the representative curves, whereas the satellite-derived crestlines are withheld from the construction step and reserved for independent evaluation. The resulting monthly coefficient tables turn leading-crestline estimation into direct polynomial evaluation, providing a compact, interpretable, and rapidly evaluable reference for the surface-expressed leading-crestline morphology. This reference supports crestline mapping, rapid forecasting of crestline position and shape, and offshore-operation planning, and complements event-resolving simulations, intermittent satellite mapping, and training-dependent data-driven models. The remainder of this paper is organized as follows. Section 2 presents the monthly climatological-mean framework, the MITgcm and satellite data, and the crestline extraction and parameterization methods. Section 3 presents the results and discussions, including the monthly coefficient tables and the independent satellite evaluation. Section 4 summarizes the conclusions.

2 Data and Methods

MITgcm-derived SSHG fields and IOCAS/MODIS satellite-derived crestlines are used for different purposes in this study. The representative curves are constructed from the MITgcm SSHG fields described in Section 2.2, including crestline extraction, aggregation by crossing longitude, and polynomial fitting (Sections 2.4–2.5). The polynomial coefficients are estimated only from the MITgcm-derived crestline ensembles. The IOCAS/MODIS crestlines described in Section 2.3 are not used in any construction step and serve only as independent, out-of-sample observations for the evaluations in Sections 3.2–3.4.

2.1 Monthly climatological-mean framework for the leading-crestline morphology

As discussed in the Introduction, the surface-expressed ISW leading-crestline morphology is influenced by bathymetric steering, vertical stratification, background circulation, and event-scale source and propagation conditions. The monthly climatological-mean framework used here targets the repeatable large-scale component of this morphology. For each calendar month, fixed bathymetry and month-specific stratification define a background propagation setting within which representative leading-crestline curves can be constructed. The parameterization is conditioned on calendar month and crossing longitude λ^*, and its variables are the sea-surface position, orientation, and curvature of the leading crestline.

Under monthly climatological stratification, the pycnocline structure for a given calendar month is prescribed. Within this condition, the pycnocline information relevant to large-scale crestline morphology is expressed through the surface signature. Surface signatures have long been used to retrieve subsurface ISW properties such as characteristic half-width and amplitude (Zheng et al., 2001), indicating that the surface expression carries quantitative information about the underlying internal wave and its stratification-conditioned structure. The present study therefore parameterizes the surface-expressed leading crestline as a two-dimensional geometric descriptor of the large-scale propagation pattern.

Event-scale currents, Kuroshio variability, mesoscale eddies, and source variability can introduce phase shifts and local crestline deformation around the monthly representative curve. Previous observations and simulations in the Luzon Strait–

https://doi.org/10.5194/egusphere-2026-4336
Preprint. Discussion started: 18 August 2026

Dongsha corridor link these processes to propagation-speed modulation, arrival-time shifts, path refraction, and localized steering (Alford et al., 2010; Park and Farmer, 2013; Li et al., 2016; Huang et al., 2024). In the present analysis, their net geometric imprint is summarized through the satellite evaluation: Section 3.3 separates the cross-front residual into a scene-level offset δ and a phase-aligned shape residual, allowing the representative curves to be assessed in terms of both bulk displacement and residual shape mismatch.

2.2 MITgcm Data

This study uses synthetic internal solitary wave scenarios from nonhydrostatic MITgcm simulations as the input source, following the configuration of Gong et al. (2023, 2025). The regional model domain covers 115.8°E to 123.8°E and 17.8°N to 22.3°N. The horizontal grid spacing is 500 m in both zonal and meridional directions, with 90 vertically stretched layers from 5 m near the sea surface to 120 m near the bottom in deep water, and a 10 s time step. Open boundaries are forced by eight barotropic tidal constituents from TPXO8, M_2, S_2, N_2, K_2, K_1, O_1, P_1, and Q_1, with a 25 km sponge layer and bathymetry interpolated from GEBCO. Constant turbulent parameters are applied as $A_h = K_h = 0.5\mathrm{m^2\,s^{-1}}$ and $A_v = K_v = 5.0 \times 10^{-3}\ \mathrm{m^2\,s^{-1}}$, and bottom stress is parameterized with a quadratic drag coefficient $C_d = 2.5 \times 10^{-3}$.

Consistent with the monthly-climatological framework described in Section 2.1, background stratification is initialized from WOA18 monthly climatology (Locarnini et al., 2019; Zweng et al., 2019), using spatially averaged monthly fields to construct horizontally uniform temperature and salinity profiles. Simulations are integrated for 15 to 30 days, with the first 3 days treated as model adjustment. Model outputs include hourly fields over the full domain. Hourly sea surface height fields are then converted to SSHG images, which highlight the surface expression of ISW leading crestlines and provide the source domain for extracting simulated leading crestlines and constructing representative curves. Figure 1 shows one representative SSHG snapshot from the August simulation at 02:00 UTC on 8 August 2014.

The employed MITgcm configuration has previously been shown to reproduce tides, crestline patterns, and key wave properties with good skill (Gong et al., 2023, 2025). Barotropic tidal comparisons against TPXO8 yield RMSE values below $0.02\mathrm{m\,s^{-1}}$ over most of the model domain. Simulated crestline patterns show good agreement with MODIS imagery in crestline length and curvature for representative events. At the DS mooring site, arrival time differences remain below 1.5 h with RMSD around 0.64 h to 0.71 h, with reported event detection rates of 8.6% false positives and 11.4% false negatives. These previous validations support the use of MITgcm-derived SSHG fields as a physically credible source domain for crestline extraction. The present study, however, evaluates the derived parameterization separately against independent satellite-derived crestlines.

https://doi.org/10.5194/egusphere-2026-4336
Preprint. Discussion started: 18 August 2026

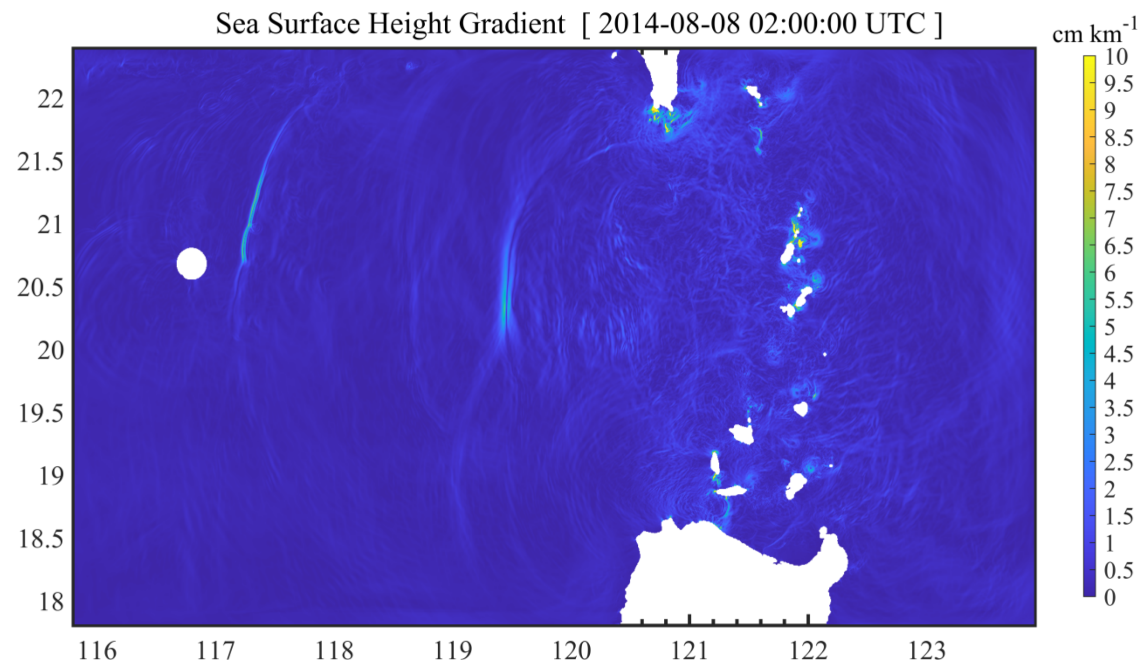

Figure 1: Sea surface height gradient computed from hourly MITgcm sea surface height at 02:00 UTC on 8 August 2014.

2.3 Remote Data

We employ remote-sensing-based crestline observations as an independent satellite-derived reference for evaluation. The crestline records used here are drawn from the Institute of Oceanology, Chinese Academy of Sciences (IOCAS) 22-year internal wave dataset for the northern South China Sea (Zhang and Li, 2024), which covers 112.40°E to 121.32°E and 18.32°N to 23.19°N over 2000 to 2022. A total of 15,830 MODIS true-color scenes were collected at 250 m resolution and distributed as GeoTIFFs with WGS84 georeferencing; 3,085 scenes were identified as containing internal wave signatures. Crestlines are extracted with the IWE-Net deep-learning model and post-processing that converts pixel-scale detections into georeferenced crest polylines. Zhang et al. (2023) report an overall mean precision, recall, and F1-score of 85.75%, 85.67%, and 85.71%, respectively, indicating stable skill for internal wave signature extraction across imaging mechanisms. For MODIS imagery in the South China Sea, Zhang and Li (2024) further report an average precision of 87.90% with about 12% false positives that are primarily caused by quasi-linear non-IW features and can be removed by manual screening. The documented quality of the IOCAS satellite crestline product justifies its adoption as an independent reference for evaluating the parameterized representative curves.

2.4 Crestline Extraction Method

To implement the monthly climatological-mean framework of Section 2.1, the MITgcm sea surface height gradient fields must first be converted into explicit crestline records that can be compared across scenes. This section describes the workflow used to extract ISW crestlines from each SSHG field. The extracted crestlines provide the direct input for the monthly aggregation

https://doi.org/10.5194/egusphere-2026-4336
Preprint. Discussion started: 18 August 2026

and mean-curve fitting described in Section 2.5. They also establish the geometric link between the model results and the remote sensing observations introduced in Section 2.3.

In SSHG imagery, the leading internal solitary wave appears as a narrow curvilinear signature. The extraction procedure is designed to retain its large-scale propagation pattern while suppressing fragmented background features and small scale noise. The workflow includes preprocessing, Canny edge detection (Canny, 1986), geometric screening, and density-based reassembly. Fig. 2 shows the preprocessing steps used to suppress noise and enhance crestline signatures. Fig. 3 presents the complete workflow from the raw SSHG field to the final extracted crestlines overlaid on the original SSHG map.

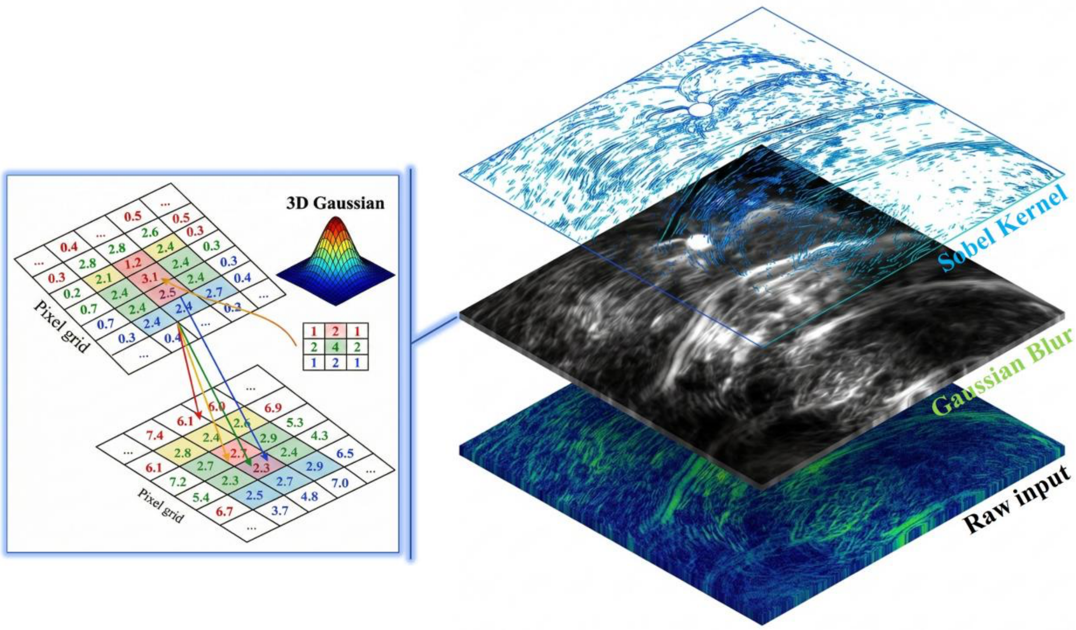

Figure 2: Illustration of the preprocessing logic used for crest extraction. Gaussian smoothing suppresses small-scale clutter and noise interference in the SSHG image, while gradient operators (e.g., Sobel kernels) sharpen the band edges associated with internal wave crests, laying the foundation for subsequent edge-based crestline detection.

Preprocessing is first applied to attenuate multi-scale background variability and intermittent sea-surface clutter. Meanwhile, crest-related band signatures are retained, including segments that are locally fragmented. Each SSHG scene is convolved with a 3×3 Gaussian kernel, normalized to $[0,1]$, and contrast-enhanced using a clipped linear stretch, $I' = \mathrm{clip}(\alpha I + \beta)$, with $\alpha = 1.5$ and $\beta = 0$. This step improves the separability between potentially weak crest signatures and background texture or noise, while constraining pixel intensities to a bounded dynamic range that stabilizes subsequent threshold based detection. In Fig. 2, the Gaussian-blurred layer suppresses high-frequency clutter, while the overlaid gradient response sharpens transitions between wave-related bands and background structures, making crest-like line features easier to isolate.

Subsequently, the crestline associated with the leading wave of each ISW packet is delineated using the Canny operator with Non-Maximum Suppression (NMS), which produces thin and precisely localized ridges. After thresholding, the detected edges mark strong SSHG gradients associated with surface convergence or divergence and are used as crestline candidates (Zhang

https://doi.org/10.5194/egusphere-2026-4336
Preprint. Discussion started: 18 August 2026

et al., 2019). To enhance robustness under variable sea surface visibility, we employ dual-threshold hysteresis in the Canny stage. For full-scene processing, thresholds are set to $T_{\text{low}} = 100$ and $T_{\text{high}} = 150$ on an 8-bit scale (approximately 39% and 59% of the dynamic range). For a narrower ROI that targets the thin internal wave crest regions of primary concern, we use $T_{\text{low}} = 80$ and $T_{\text{high}} = 200$ (approximately 31% and 78%). The higher threshold identifies confident "seed" pixels exhibiting the strongest consistency with coherent internal wave signatures, whereas the lower threshold admits weaker adjacent pixels only when connected to a seed. This dual-threshold strategy helps maintain crest continuity across locally weak segments while reducing spurious edge growth arising from background variability (Kurekin et al., 2020). The principal Canny operations are summarized schematically in Fig. 3.

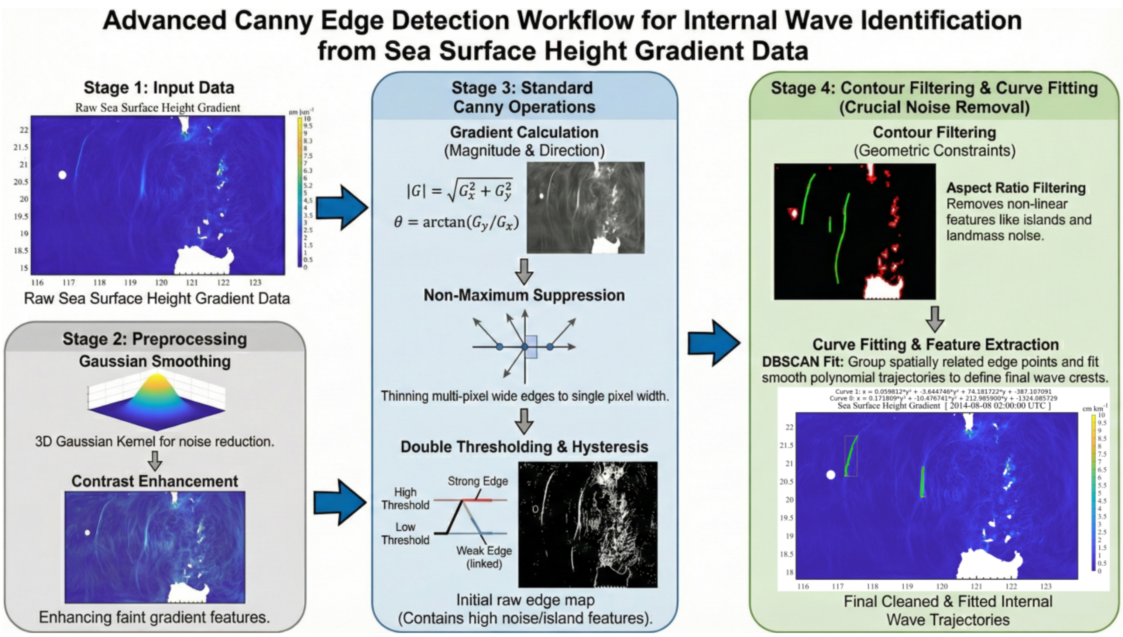

Figure 3: Workflow of the advanced Canny edge detection for internal wave identification from sea surface height gradient data, comprising four stages: (1) input of raw SSHG data, (2) preprocessing with Gaussian smoothing and contrast enhancement, (3) standard Canny operations including gradient calculation, non-maximum suppression, and dual-threshold hysteresis, and (4) contour filtering with geometric constraints and curve fitting via DBSCAN clustering and polynomial trajectory fitting.

The raw edge map still contains spurious detections unrelated to internal waves, such as coastline boundaries, island edges, and transient features like ship wakes and wind streaks. A geometric filtering step is therefore introduced prior to clustering: candidate contours are filtered based on expected ISW morphology in the northern South China Sea, where dominant propagation is westward and crests are typically meridionally elongated. Contours with bounding-box aspect ratio $w/h > 0.5$ are rejected, and a minimum arc length of 1000 pixels is required. Contours with bounding-box aspect ratio w/h > 0.5 are rejected, and a minimum arc length of roughly 170–180 km (estimated from the georeferenced SSHG axes) is required. This removes near-horizontal structures, compact land-related fragments, and short transient features. With non-ISW contours removed, the remaining edges are prepared for DBSCAN-based clustering (Ester et al., 1996). The surviving edge pixels are then transformed from image coordinates to geographic coordinates (λ, ϕ) and reassembled into coherent crest objects using

https://doi.org/10.5194/egusphere-2026-4336
Preprint. Discussion started: 18 August 2026

DBSCAN with $\varepsilon = 0.02^{\circ}$ and min_samples $= 5$. Within the study domain at 18°–22°N, ε corresponds to approximately 2 km, sufficient to bridge small gaps along a single crest while remaining below typical inter-packet separations. Each cluster is represented as a smooth crest trajectory, yielding the final crestline vectors shown in Fig. 3. These vectors form the standardized vector input for subsequent compositing, curve modeling, and comparison with crestlines identified from satellite imagery.

2.5 Construction and Parameterization of Representative Crestlines

To examine whether leading crestlines passing through similar locations share a repeatable large-scale shape, each extracted crestline is indexed by the longitude at which it crosses the reference latitude of 20.6°N, denoted as the crossing longitude λ^*. The latitude 20.6°N is chosen because a zonal transect at this latitude intersects nearly all leading crestlines within the study corridor, so that every crestline receives a well-defined λ^*; any other latitude with this property would serve equally well and would yield consistent binning. Because ISW packets in this corridor propagate predominantly westward from the Luzon Strait, λ^* decreases monotonically as a wave propagates, and it therefore serves as a natural proxy for the propagation stage of a crestline along the corridor: crestlines with similar λ^* have traversed similar bathymetry and stratification and are expected to exhibit similar large-scale shapes. Each crestline is then assigned to a location bin by rounding λ^* to the nearest 0.1°. This λ^*-based grouping gathers complete crestline trajectories from different scenes and times into ensembles occupying the same along-corridor position. Figure 4 illustrates the construction: when crestlines within the same λ^* bin are superimposed, they form a large-scale envelope with coherent curvature, despite event-to-event scatter and occasional incomplete extraction in individual scenes. In most bins, the spread of crest positions relative to the bin-mean curve remains within a few kilometers over the 18°–22°N latitude range. This repeatable feature motivates representing each bin by an analytical, month-specific representative curve, providing a compact analytical representation of the leading-crestline shape.

https://doi.org/10.5194/egusphere-2026-4336
Preprint. Discussion started: 18 August 2026

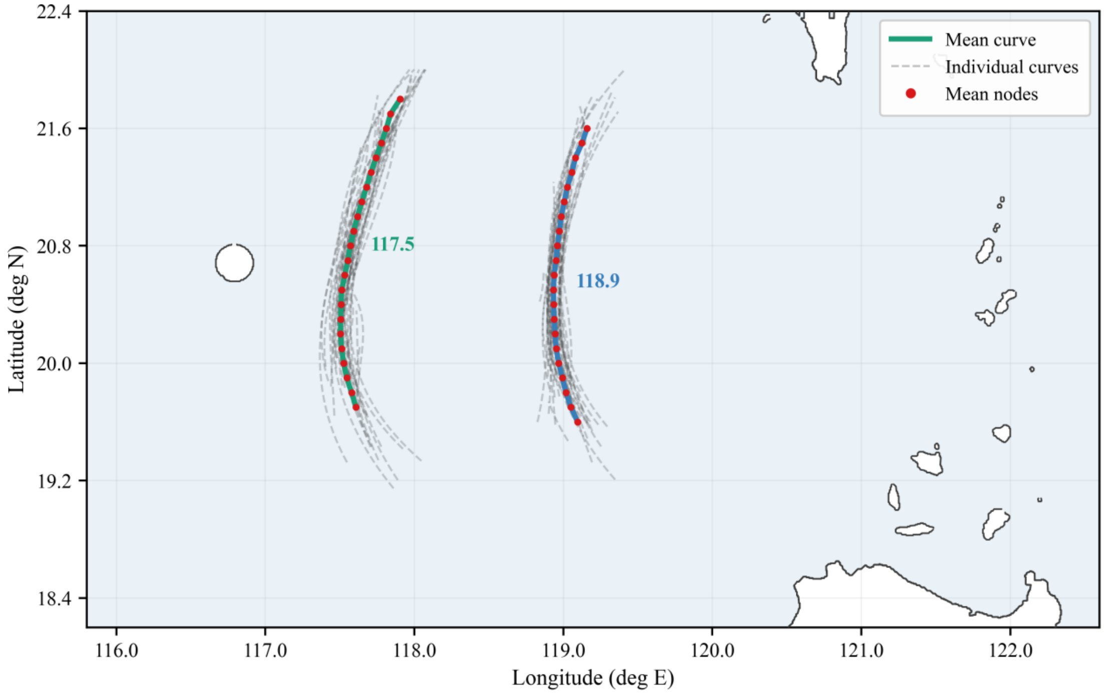

Figure 4: Monthly aggregation and mean-curve construction for two representative longitude bins ($\lambda^* = 117.5^{\circ}$E and 118.9°E). Gray dashed lines show individual crestlines within the month; red dots denote retained mean nodes on the latitude grid; the solid green and blue curves show the fitted cubic representative curve.

Further examination of the cluster-mean curves shows that a low-order polynomial provides a practical empirical representation of the systematic curvature within each bin. Under the monthly-climatological pycnocline, refraction over the continental slope and diffraction around Dongsha topography can impose smooth, large-scale bending on the wavefront; the resulting crestline often exhibits one inflection where the refraction gradient changes sign along the propagation corridor. A cubic polynomial is the minimum-degree polynomial that can accommodate both variable curvature and a single inflection, whereas a quadratic form enforces curvature of one sign only. Fitting trials across all λ^* bins and months indicate that the cubic form provides a stable representation of the cluster-mean nodes (Section 3.1). The representative curve is therefore parameterized as longitude as a function of latitude,

$$\mathrm{Lon}(\mathrm{Lat}) = C_0\mathrm{Lat}^3 + C_1\mathrm{Lat}^2 + C_2\mathrm{Lat} + C_3, \tag{1}$$

where Lon is longitude (°E), Lat is latitude (°N), and $\{C_0, C_1, C_2, C_3\}$ are the coefficients of the monthly representative curve. The cubic polynomial is used as an empirical low-order geometric representation of the surface-expressed leading crestline, rather than as a dynamical law for ISW propagation. Once these four coefficients are determined for a specific month and λ^* bin, the representative curve can be evaluated by direct polynomial substitution.

To confirm quantitatively that the cubic order is adequate—neither under- nor over-parameterized—the out-of-sample predictive value of each additional polynomial order was assessed by leave-one-node-out cross-validation (LOOCV). For this

https://doi.org/10.5194/egusphere-2026-4336
Preprint. Discussion started: 18 August 2026

order-selection test, the extracted August crestlines were grouped into 69 year × λ^* bins (23, 21, and 25 bins from the August datasets of 2014, 2015, and 2022, respectively), so that each cross-validated node curve corresponds to a single independent fitting unit; this grouping is used only for the cross-validation statistics, and the representative curves themselves remain fitted to the pooled August ensembles (Section 2.5). Within each bin, each retained mean node was held out in turn, a polynomial of degree 1–4 was refitted to the remaining nodes, and the held-out node was predicted (Fig. 5). Raising the order from 1 to 2 and from 2 to 3 reduced the cross-bin median LOOCV RMSE by 77.6% (95% bootstrap confidence interval, 63.2–82.6%) and 29.1% (CI, 15.8–39.5%), respectively, with both intervals excluding zero. In contrast, the improvement from degree 3 to degree 4 was not significant (12.5%, CI −2.6 to 24.7%, spanning zero), and near the latitude endpoints of the node curves, where the fit is least constrained, the quartic point estimate was in fact worse than the cubic (−6.9%, CI −27.0 to 19.1%; not shown in Fig. 5). The cubic is therefore retained: each step up to degree 3 yields a reliable out-of-sample gain, whereas a fourth order adds no significant overall benefit and degrades the edge behaviour of the fitted curves.

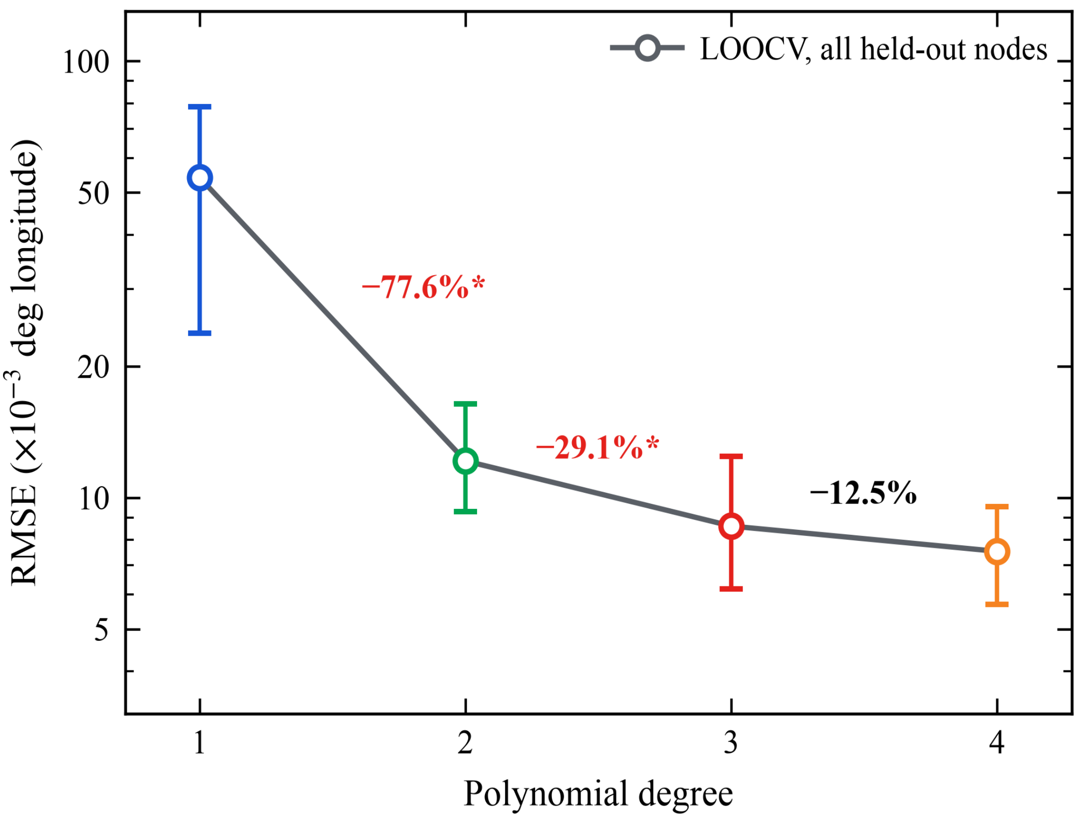

Figure 5: Out-of-sample order selection for the representative-curve polynomial. Circles show the median leave-one-node-out cross-validation (LOOCV) RMSE in longitude across the 69 August year × λ^* bins (23, 21, and 25 bins from the August datasets of 2014, 2015, and 2022, respectively; bars: interquartile range), for polynomial degrees 1–4 of Lon(Lat). Labels give the change in the cross-bin median RMSE at each consecutive step, with 95% confidence intervals from 20,000 paired bootstrap resamples of the bins. Asterisks mark steps whose interval excludes zero (1→2: −77.6%, CI 63.2–82.6%; 2→3: −29.1%, CI 15.8–39.5%); the degree-3-to-degree-4 step (−12.5%, CI −2.6 to 24.7%) is not significant. Successive out-of-sample gains are therefore significant up to the cubic and not beyond.

https://doi.org/10.5194/egusphere-2026-4336
Preprint. Discussion started: 18 August 2026

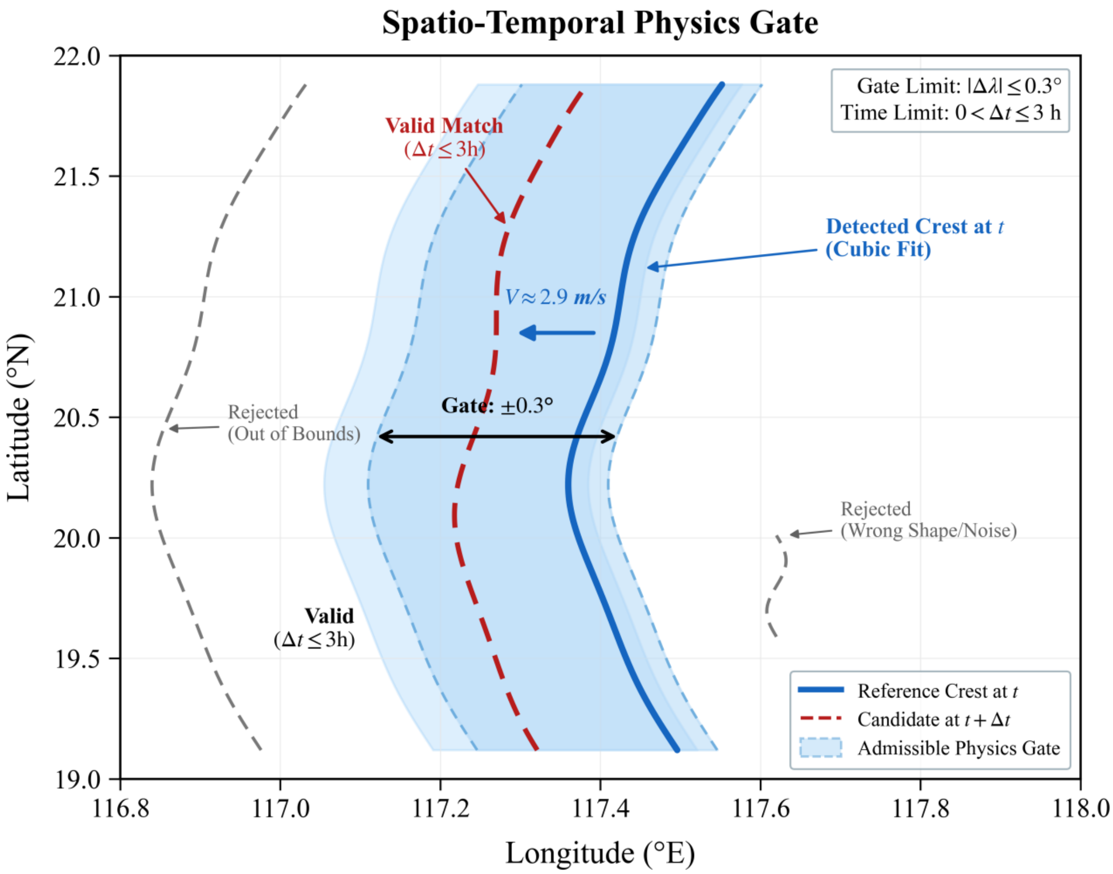

**Figure 6: Schematic of the spatiotemporal association criterion used for crest matching. A candidate crest at $t + \Delta t$ (red dashed) is linked to the reference crest at t (blue) only if it falls within the admissible band (light blue), defined by $0 < \Delta t \leq 3$h and $|\Delta\lambda^*| \leq$
280 0.3°. Gray examples illustrate rejected candidates that either exceed the spatial bound or exhibit inconsistent morphology.**

The following details supplement the clustering and binning procedure. In addition to the spatial binning, crest records within each λ^* bin are ordered by acquisition time and linked only when a conservative spatiotemporal feasibility bound is satisfied:

$$0 < \Delta t \leq 3\text{h}, |\Delta\lambda^*| \leq 0.3^{\circ}. \tag{2}$$

Over $18^{\circ} - 22^{\circ}$ N, 0.3° corresponds to roughly 31–32 km. This bound implies an admissible apparent translation of approximately 2.9–3.0ms^{-1} over 3 h, which is consistent with reported speeds for strong, nonlinear ISWs and internal-tide fronts in this corridor (Zhao and Alford, 2006). Since the ISWs in this corridor propagate predominantly westward, $\Delta\lambda^*$ should be negative under ideal conditions. However, we employ the absolute value $|\Delta\lambda^*|$ in the association criterion to accommodate occasional sign reversals arising from crest-extraction noise and latitude-dependent offsets introduced by crestline curvature. This spatiotemporal matching criterion thus establishes a conservative feasibility bound with an explicit error tolerance, effectively filtering out spurious associations between distinct wave trains prior to monthly averaging. The mean crestline position is then computed on a fixed latitude grid with 0.1° spacing. A node is retained if either (i) the contributing count

https://doi.org/10.5194/egusphere-2026-4336
Preprint. Discussion started: 18 August 2026

exceeds 50% of all crestlines in the same λ^* bin, or (ii) the absolute count reaches $n \geq 10$. This threshold prevents sparsely sampled or fragment-dominated nodes from biasing the mean curve. Fig. 6 provides a schematic view of the admissible spatiotemporal association criterion.

The same aggregation procedure is applied only to the region east of Dongsha Atoll, where the propagation pathway remains sufficiently coherent to support robust mean curve construction, and Fig. 4 shows two representative examples. This regional restriction reflects the physical complexity that develops at and beyond the atoll. A westward-propagating ISW encountering Dongsha can bifurcate into northern and southern branches that reconverge on the western side, generating complex nonlinear wave interactions (Li et al., 2013). Subsequent remote sensing analyses and numerical simulations confirm that similar complex interaction patterns occur frequently around and south of the atoll through diffraction and refraction of incoming crests (Z. Zeng et al., 2024; Jia et al., 2018). Farther shoreward, shoaling induces waveform deformation, fission, instability, and enhanced mixing, making the morphology progressively less suited to representation by a single smooth mean curve (Song et al., 2021; Meng et al., 2024). The observational coverage from the Luzon Strait to Dongsha Atoll is also far denser than that west of Dongsha, further supporting a separate treatment of the western sector (Chen et al., 2019). Therefore, the present representative-curve construction is applied to the coherent east-of-Dongsha propagation corridor, where the propagation pathway remains sufficiently organized to support robust monthly mean-curve construction.

3 Results and discussions

This section presents and discusses the monthly representative curves of surface-expressed leading ISW crestlines. Section 3.1 presents the monthly coefficient-table output, with the August table shown as a representative example (Table 1). Section 3.2 evaluates the August representative curves against independent IOCAS/MODIS crestlines along the Luzon Strait to Dongsha corridor, and Section 3.3 examines the phase-offset and shape-residual structure of the evaluation. Section 3.4 reports independent case-level evaluations for three additional calendar months, in which each satellite case is compared with the representative curves of its own month.

3.1 Monthly representative leading-crestline curves

Because the workflow of Sections 2.4–2.5 operates under WOA18 monthly climatological stratification, it was applied to each of the 12 calendar months, yielding a month-specific coefficient table for every month. In this paper, the August table is presented as the representative output and is used for the primary satellite evaluation.

Each row in a coefficient table corresponds to the representative crestline curve of one λ^* bin. The four coefficients $\{C_0, C_1, C_2, C_3\}$ define the cubic polynomial $\mathrm{Lon} = C_0\mathrm{Lat}^3 + C_1\mathrm{Lat}^2 + C_2\mathrm{Lat} + C_3$, and $\mathrm{Lat}_{\min}$ and $\mathrm{Lat}_{\max}$ give the supported latitude interval of that curve.

https://doi.org/10.5194/egusphere-2026-4336
Preprint. Discussion started: 18 August 2026

Longitude (°E)	C_0 ($\times 10^{-2}$)	C_1	C_2	C_3	$\mathrm{Lat}_{\mathrm{min}}$ (°N)	$\mathrm{Lat}_{\mathrm{max}}$ (°N)
118.8	-0.90	4.499	-7.42	819.58	19.7	21.4
118.6	-0.31	6.557	-38.90	1098.23	19.7	21.5
118.4	-0.12	1.531	-6.03	396.34	19.6	21.7
118.2	-0.58	1.807	-1.54	432.79	19.6	21.8
118.0	-0.10	2.114	-7.63	472.96	19.6	22.0
117.9	-0.23	0.961	-3.85	309.33	19.8	22.0
117.7	0.55	-0.160	-0.34	144.62	19.8	22.0
117.5	-0.08	0.253	-0.34	209.79	19.8	22.0
117.3	-0.29	2.774	-9.57	542.48	19.7	21.5
117.1	1.61	-0.863	15.13	30.47	20.0	21.7
117.0	3.52	-2.064	40.40	-246.81	20.1	21.8

Table 1: Coefficients of the August representative leading-crestline curves east of Dongsha Atoll. Each row gives the cubic coefficients for the representative curve of one λ^* bin and the latitude interval over which the curve is supported by the composited crestline ensemble.

To apply a monthly coefficient table, the λ^* bin corresponding to the target location is selected, and the representative crestline is then obtained by evaluating the listed cubic polynomial within its supported latitude range; Table 1 illustrates this for August. The physical content of these coefficient tables deserves emphasis. The SSHG source fields are generated by nonhydrostatic MITgcm simulations over realistic GEBCO bathymetry under WOA18 monthly climatological stratification (Section 2.2), so the extracted crestlines inherit the two principal background controls represented in the present framework: bathymetric steering and the month-specific pycnocline structure. The resulting background propagation-speed field, governed by the prescribed stratification and spatially varying water depth, contributes to the large-scale bending of the crestlines (Zhao and Alford, 2006; Alford et al., 2015), and because these background fields are fixed within each calendar month, crestlines crossing the same λ^* are dynamically conditioned, rather than merely grouped statistically, to cluster around a common large-scale morphology (Fig. 4; Table 1). Since the bathymetry is identical across all 12 calendar months, differences among the monthly coefficient tables are primarily associated with the month-specific stratification, which provides the physical basis for comparing each observed crestline with the representative curves of its own calendar month (Section 3.4).

3.2 Independent satellite evaluation of the August representative curves

This section evaluates the August representative curves against independent IOCAS/MODIS crestlines. Nine independent August evaluation cases are drawn from MODIS scenes acquired in 2014, 2015, and 2022 within the Luzon Strait–Dongsha corridor (Figs. 7–12).

https://doi.org/10.5194/egusphere-2026-4336
Preprint. Discussion started: 18 August 2026

Fig. 7 presents representative satellite-overlay examples for the August primary demonstration. Throughout the evaluation, each evaluated crestline object is labeled by the acquisition date of its MODIS scene (YYYYMMDD) followed by a two-digit sequence number, so that multiple independent wave-packet objects identified in the same scene receive distinct labels. The 14 August 2022 scene illustrates the evaluation setting, in which two evaluated crestline objects, 2022081401 and 2022081402, are associated with the August 117.0°E and 118.4°E representative curves, respectively. These two objects are distinct evaluated crestlines (wave packets) identified in the same scene rather than duplicate records. The 117.0°E object lies near Dongsha Atoll, where local refraction and multi-crest structure complicate crest matching, whereas the 118.4°E object lies farther east, where partial cloud cover interrupts the satellite signature and the continuous representative curve supplies a continuous shape reference across the obscured segment.

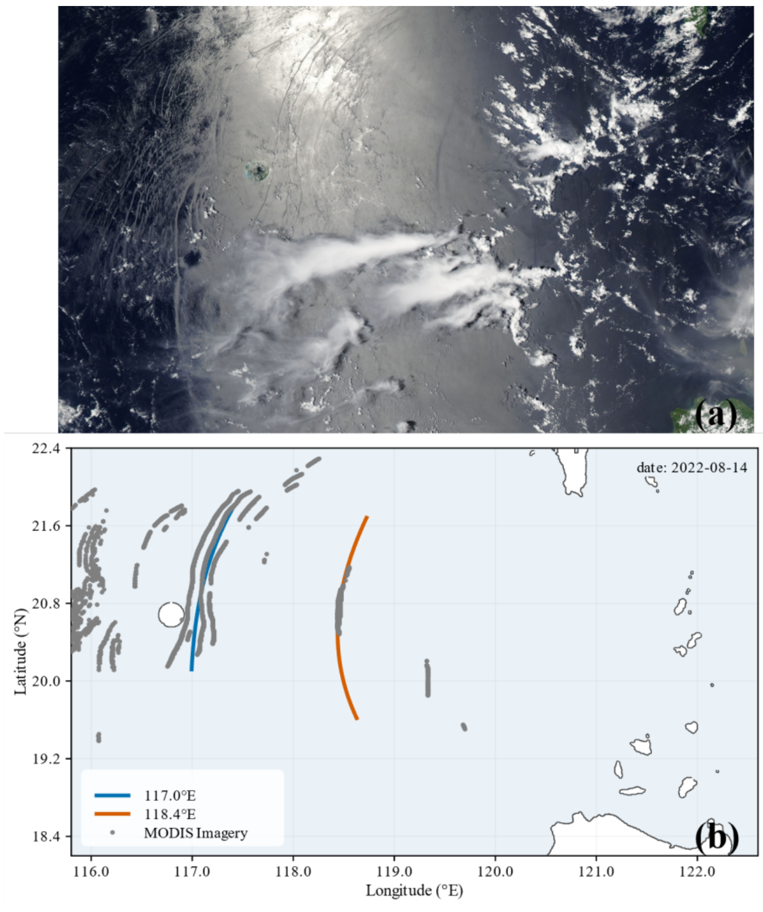

Figure 7: Representative satellite-overlay examples for the August primary demonstration. The 14 August 2022 scene includes two evaluated crestline objects (2022081401 and 2022081402) associated with the 117.0°E and 118.4°E representative curves. Gray signatures denote MODIS-extracted crestline observations, and colored curves denote the corresponding monthly representative leading-crestline curves.

https://doi.org/10.5194/egusphere-2026-4336
Preprint. Discussion started: 18 August 2026

To quantify geometric agreement, satellite-derived crest points were first binned by latitude so that densely sampled segments did not dominate the statistics, with one representative point retained per latitude bin. At each latitude Lat_i, the observed longitude was compared with the longitude predicted by the representative curve:

$$\Delta\mathrm{Lon}_i = \mathrm{Lon}_{\mathrm{sat},i} - \mathrm{Lon}_{\mathrm{pred}}(\mathrm{Lat}_i), \quad (3)$$

where $\mathrm{Lon}_{\mathrm{sat},i}$ is the longitude of the binned satellite-derived crest point at Lat_i, and $\mathrm{Lon}_{\mathrm{pred}}(\mathrm{Lat}_i)$ is the longitude predicted by the representative curve at the same latitude. Before calculating the evaluation metrics, the corresponding coordinates were transformed from longitude–latitude coordinates to Universal Transverse Mercator (UTM) Zone 50N (EPSG:32650), which corresponds to the standard UTM zone for the 114°–120°E longitude band and covers the region containing the evaluated crestlines. Because a given longitude difference represents different ground distances at different latitudes, this transformation places all comparisons on a common metric scale, making the error calculation more direct and the graphical comparison easier to interpret. The residual used in the statistical calculations was therefore evaluated as

$$\Delta\mathrm{Lon}_i = x^{\mathrm{UTM}}_{\mathrm{sat},i} - x^{\mathrm{UTM}}_{\mathrm{pred}}(\mathrm{Lat}_i), \quad (4)$$

where $x^{\mathrm{UTM}}_{\mathrm{sat},i}$ and $x^{\mathrm{UTM}}_{\mathrm{pred}}(\mathrm{Lat}_i)$ are the UTM eastings, in meters, of the satellite-derived crest point and the predicted representative curve, respectively, so that the calculated residual is the metric distance derived from a same-latitude longitudinal comparison.

The overall mismatch along each crestline was quantified using the root-mean-square error:

$$\mathrm{RMSE}_{\Delta\mathrm{Lon}} = \sqrt{\frac{1}{N}\sum_{i=1}^{N} (\Delta\mathrm{Lon}_i)^2}, \quad (5)$$

where N is the number of retained latitude bins. Because $\Delta\mathrm{Lon}_i$ is evaluated from the projected UTM eastings, $\mathrm{RMSE}_{\Delta\mathrm{Lon}}$ is a metric distance and is reported in meters. Additional skill metrics, including Mean Absolute Error (MAE), R^2, Nash–Sutcliffe Efficiency (NSE), Willmott's index of agreement (d), Kling–Gupta Efficiency (KGE), and Pearson's r, were calculated from the same residual sequence using their standard definitions.

Figure 8 presents the predicted representative curves and the corresponding satellite-derived crest points in the projected UTM coordinate frame (Zone 50N, EPSG:32650). In this coordinate system, northing is the metric distance north of the Equator, and easting follows the standard UTM false-easting convention: the central meridian at 117°E is assigned an easting of 500 km rather than 0 km, so that easting values remain positive throughout the zone. Equivalently, the easting origin (0 km) lies 500 km west of 117°E, near 112°E at the study latitudes (approximately 112.2°E at 20.6°N). The easting values on the horizontal axes are therefore metric distances east of this ~112°E reference: the 500-km tick marks the 117°E central meridian, the western boundary of the east-of-Dongsha analysis segment (117°E–119°E), and the evaluated crestlines fall at eastings of approximately 450–700 km. The calculations were performed in meters, whereas easting and northing are displayed in kilometers for readability. Each panel reports N, $\mathrm{RMSE}_{\Delta\mathrm{Lon}}$, and R^2.

https://doi.org/10.5194/egusphere-2026-4336
Preprint. Discussion started: 18 August 2026

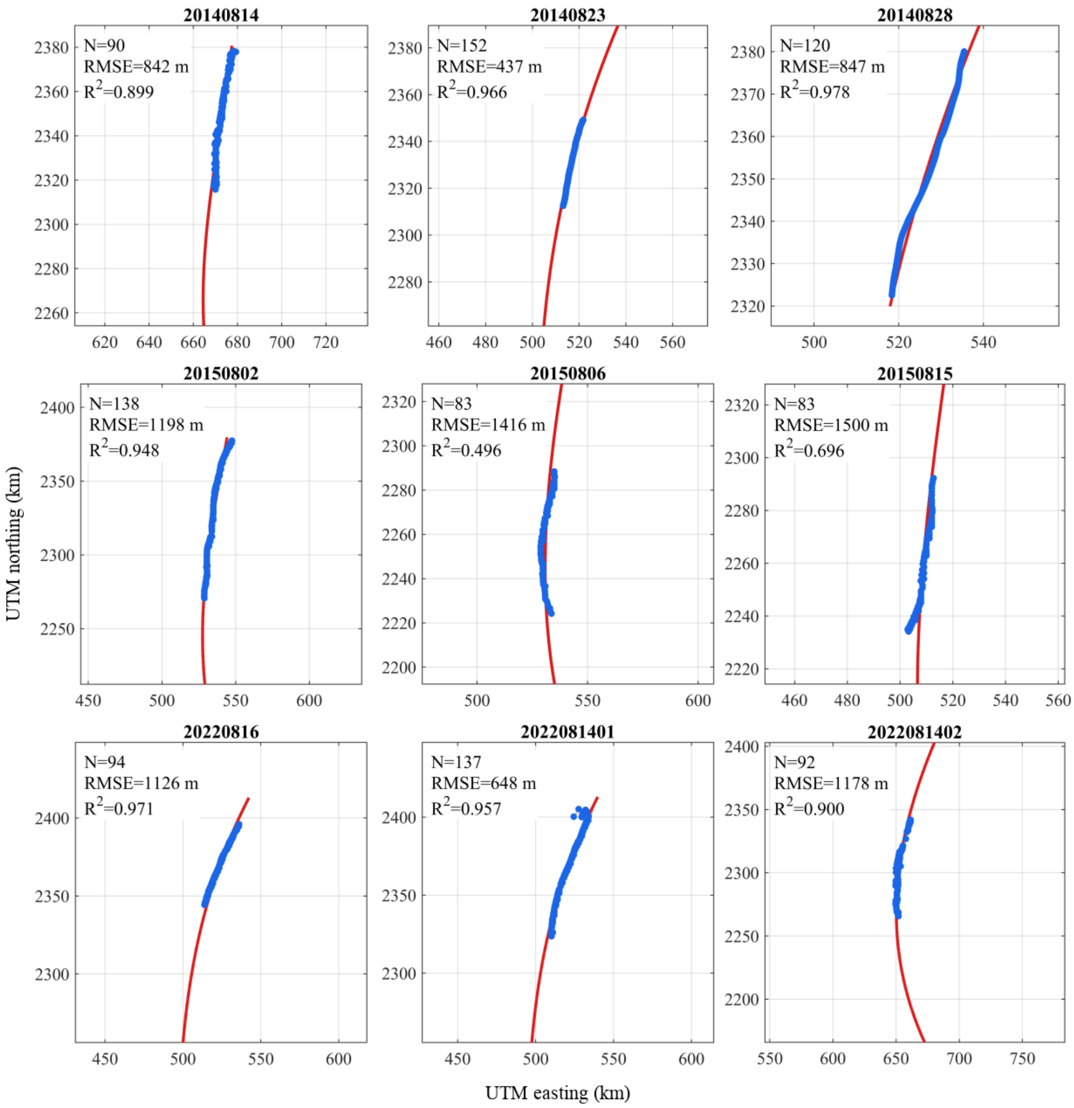

385 **Figure 8: Evaluation of the August representative curves against nine independent satellite-derived crestline cases from 2014, 2015, and 2022. Coordinates are shown in Universal Transverse Mercator (UTM) Zone 50N (EPSG:32650), with easting and northing expressed in kilometers. Northing is the metric distance north of the Equator; easting follows the standard UTM false-easting convention, with the 117°E central meridian assigned an easting of 500 km, so the easting origin (0 km) lies 500 km west of 117°E, near 112°E at these latitudes. Axis ticks such as 450 and 500 km thus denote metric distances east of this reference, the 500-km tick**
390 **marking 117°E at the western boundary of the analysis segment (117°E–119°E); the evaluated crestlines lie at eastings of about 450–700 km. Each panel is cropped to the local extent of the evaluated crestline. Red curves show the predicted representative crestline morphology, and blue points show the satellite-derived crest observations. Each panel reports *N*, RMSE$_{\Delta Lon}$, and R^2.**

Across the nine evaluation cases, the predicted representative curves reproduce the dominant spatial variation of crest position along the observed fronts, although localized departures occur in several scenes. The ensemble statistics are summarized in
395 Fig. 9.

https://doi.org/10.5194/egusphere-2026-4336
Preprint. Discussion started: 18 August 2026

The mean Pearson correlation reaches $r = 0.968$, indicating that the representative curves reproduce the dominant spatial variation of crest position along the front in the tested August scenes. The mean error magnitudes are $\mathrm{RMSE}_{\Delta\mathrm{Lon}} = 1021$ m and MAE = 796 m. Willmott's index of agreement is high ($d = 0.942$), the mean R^2 and NSE reach 0.870 and 0.873, and the mean Kling–Gupta efficiency is KGE = 0.789. Together, these metrics indicate that the August representative curves reproduce the large-scale surface-expressed leading-crestline shape with kilometer-scale residuals in the tested August cases.

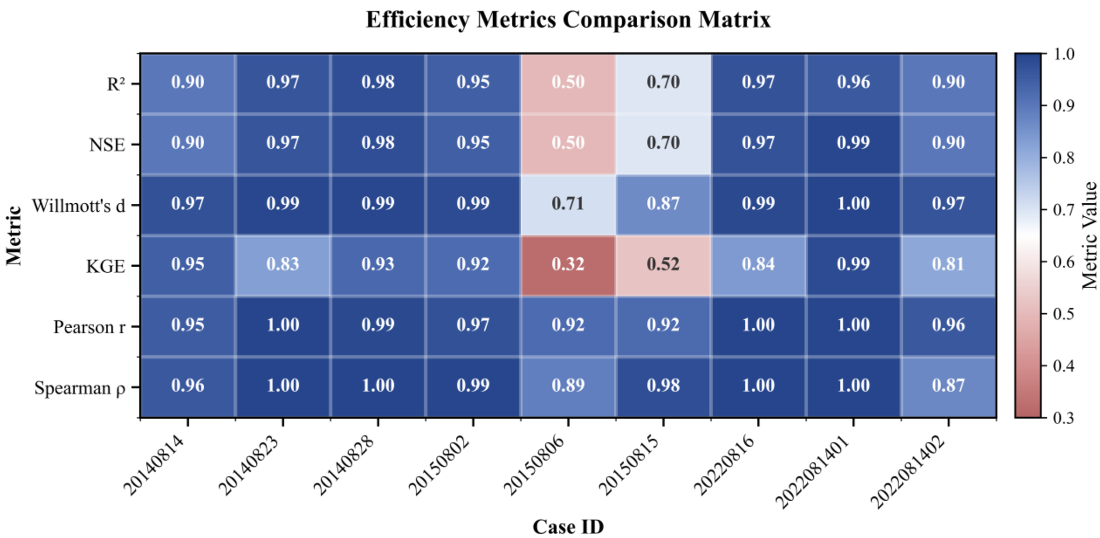

Figure 9: Summary of validation metrics for nine independent August scenes.

To place these dimensional errors in physical context, the residuals can be nondimensionalized by the characteristic length scales of the wave field itself. Normalized by typical ISW crest-to-crest separations in this corridor (5–20 km), the mean $\mathrm{RMSE}_{\Delta\mathrm{Lon}}$ corresponds to a relative error of about 0.05–0.20, i.e., roughly one-twentieth to one-fifth of the spacing between successive crests in a packet. Using a midrange 10-km packet spacing gives a relative error close to 0.10. Normalized instead by characteristic soliton half-widths reported for the northern South China Sea, which are of order 1 km (Zheng et al., 2001; Song et al., 2021), the ratio is of order unity: the representative curve locates the observed leading crest at approximately the intrinsic horizontal scale of the wave profile. In dimensionless terms, the mean shape error is smaller than the packet-scale crest spacing and comparable to the intrinsic horizontal scale of an individual soliton.

The inter-metric correlation analysis in Fig. 10 examines how the validation metrics relate to one another across the nine scenes, with the metrics grouped by role: sampling (the number of binned points N), phase (the scene-level offset magnitude $|\delta|$), error (RMSE, MAE), and skill (R^2, KGE, Pearson r). For each scene, δ is defined as the average of the residuals $\Delta\mathrm{Lon}_i$, $\delta = \frac{1}{N}\sum_{i=1}^{N} \Delta\mathrm{Lon}_i$, and represents a uniform shift of the entire observed crestline relative to the representative curve. Three patterns emerge. First, the metrics within each group are consistent: RMSE and MAE are very strongly correlated ($r = 0.97$), and the three skill metrics show high inter-correlation ($r = 0.77$–0.96), while error and skill metrics exhibit inverse relationships ($|r| =$

https://doi.org/10.5194/egusphere-2026-4336
Preprint. Discussion started: 18 August 2026

0.68–0.75). The skill assessment is therefore not driven by a single efficiency metric, and RMSE is adopted as the primary error measure. Second, sample size N correlates with lower error ($r = -0.73$ to -0.76) and higher skill ($r = 0.57$–0.73), indicating that denser along-crest sampling is associated with more representative validation statistics. Third, the phase-offset magnitude $|\delta|$ is weakly correlated with all shape-error and skill metrics ($|r| \leq 0.35$), suggesting that scene-level spatial displacement and morphology-related error behave as largely separate components. This pattern motivates the two-stage evaluation adopted in Section 3.3, in which the scene-level offset is removed first and shape fidelity is assessed on the aligned residuals.

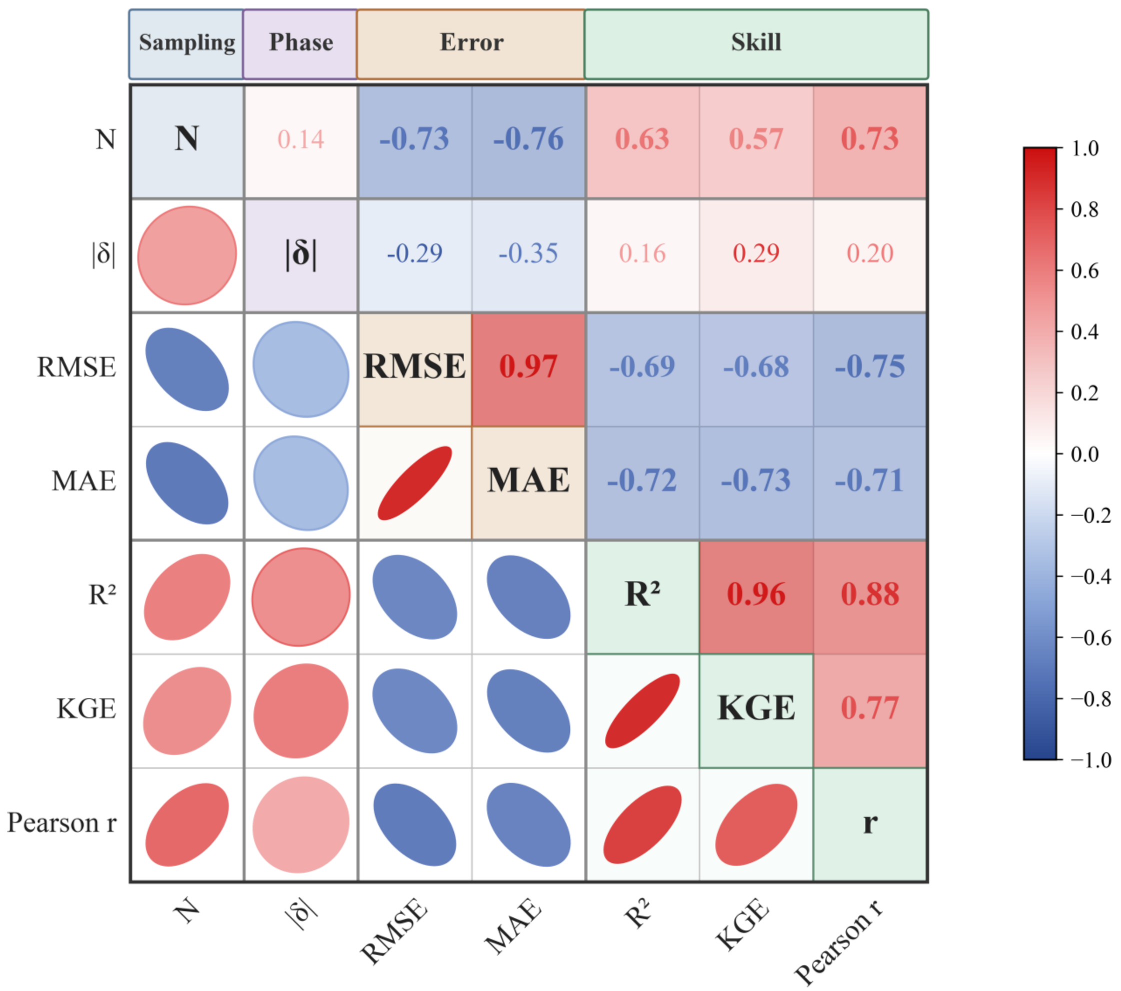

Figure 10: Inter-metric correlation matrix across the nine August scenes, with metrics grouped by role: sampling (N), phase offset ($|\delta|$), error (RMSE, MAE), and skill (R^2, KGE, Pearson r). The within-group coherence of error and skill metrics and the weak correlation of $|\delta|$ with all shape metrics support the phase-alignment-then-shape evaluation used in Section 3.3.

https://doi.org/10.5194/egusphere-2026-4336
Preprint. Discussion started: 18 August 2026

The summary metrics above describe average performance but do not show how errors distribute within each scene. Section 3.3 therefore examines the phase-aligned residual distributions, identifies the long-tailed cases, quantifies uncertainty, and revisits the remaining phase behavior.

3.3 Residual and phase-offset analysis

Motivated by the decoupling between the scene-level offset and the shape metrics identified in Section 3.2 (Fig. 10), the cross-front residual $\Delta\mathrm{Lon}_i$ is decomposed into a scene-level translational component δ (defined in Section 3.2) and a pointwise shape residual $\Delta E_i = \Delta\mathrm{Lon}_i - \delta$. This decomposition separates the scene-level offset between the parameterized representative curve and the satellite-derived crestline from the residual curvature mismatch and local geometric distortion, and it is consistent with the physical structure of the problem: event-scale currents, eddies, and source variability can displace the crestline as a whole and deform it locally, and the decomposition distinguishes their scene-level and residual manifestations so that the monthly representative curve can be assessed in terms of the large-scale shape it is designed to capture.

Fig. 11 displays the distribution of ΔE as violin-box plots for each August scene. Seven of the nine scenes show residuals concentrated around zero, with interquartile ranges of roughly $\pm$0.5–1 km and medians near zero. For these scenes, much of the raw error is a scene-level crestline shift; once that shift is removed, the representative curve reproduces the observed large-scale curvature at approximately 1 km accuracy. The residual spread reflects the discrete and sometimes fragmented nature of satellite crest extraction, as well as the difference between a monthly representative curve and the actual event-specific crestline.

https://doi.org/10.5194/egusphere-2026-4336
Preprint. Discussion started: 18 August 2026

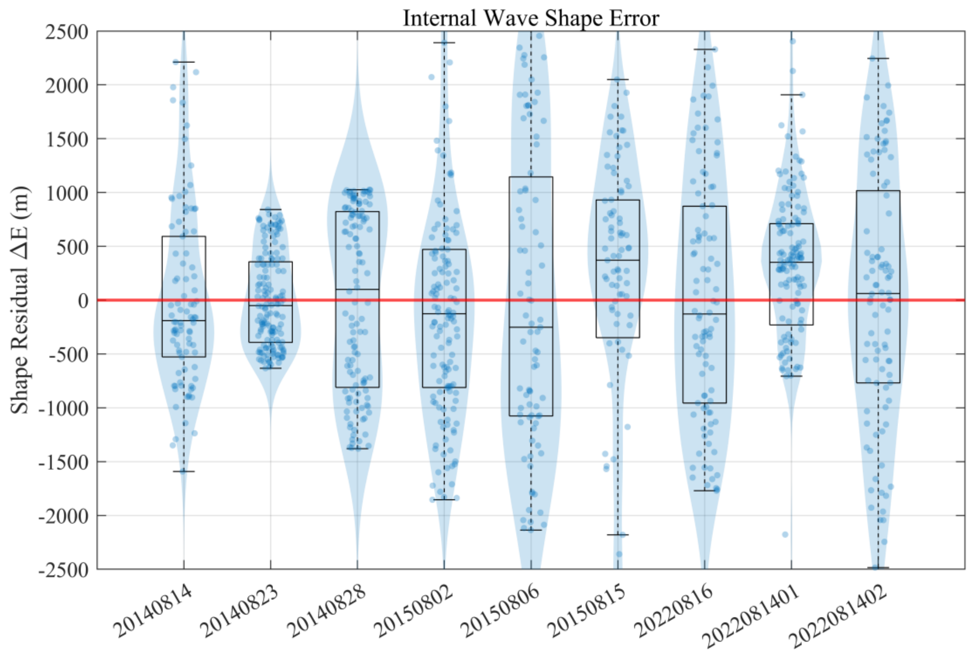

Figure 11: Phase-aligned shape residuals ΔE for nine satellite scenes. Violin-box plots summarize the residual distribution after removing the scene-level phase offset. The red line marks $\Delta E = 0$. Heavy-tailed cases (notably 20150806 and 20150815) indicate localized geometric distortions beyond uniform translation.

Cases 20150806 and 20150815 depart from this pattern, with residual distributions whose heavy tails extend into the multi-kilometer range. Both scenes retain strong Pearson correlations ($r > 0.92$), yet their variance-based efficiencies drop to $R^2 \approx$ 0.50–0.70. This combination is informative: the monotonic ordering of crest position along latitude is preserved, so the representative curve still tracks the overall crestline, while localized crest segments are deformed enough to inflate the cross-front variance. For 20150806, the MODIS imagery shows a pronounced mid-crest bend near the center of the evaluated segment (Fig. 8), indicating a localized event-scale deformation of the crestline relative to the monthly-climatological representative curve. Such kilometre-scale kinks are consistent with transient processes that the climatological framework averages into the monthly reference state, including localized current shear, eddy-induced steering, or interaction with a neighboring crest. Away from the bend, the 20150806 residuals return to the sub-kilometer level typical of the other scenes, showing that the deformation is spatially confined rather than a mismatch of the representative curve as a whole.

Pooling all phase-aligned residuals across the nine scenes yields $\mathrm{RMSE}_{\mathrm{shape}} = 1004$ m, the root-mean-square of the bias-removed shape residuals ΔE_i (Fig. 12a). Hierarchical bootstrap resampling (Saravanan et al., 2020), first across scenes to capture inter-date variability and then across points to avoid overcounting spatially correlated samples along a single crest, gives a 95% confidence interval of 787–1220 m. This places shape-representation accuracy at the approximately 1 km scale for the August validation set. Most scene-level phase lags δ fall within ±1 km, and the ensemble mean is $\overline{\delta} = -579$ m (Fig. 12b). The negative sign indicates that observed crestlines tend to lie slightly west of the representative-curve positions, a

https://doi.org/10.5194/egusphere-2026-4336
Preprint. Discussion started: 18 August 2026

pattern consistent with event-specific propagation environments running slightly ahead of the monthly-climatological mean; excluding the outlier scene 2022081401, the mean lag shrinks to −226 m, i.e., below a quarter of the shape RMSE.

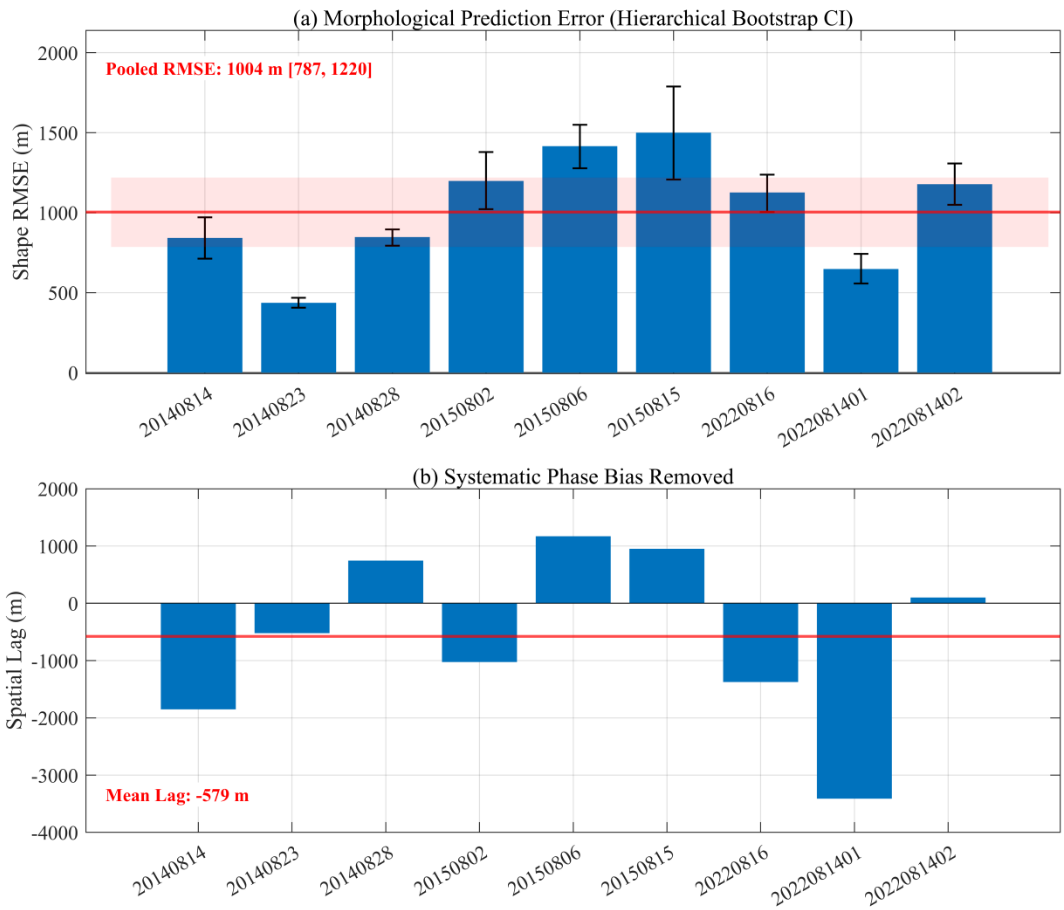

Figure 12: Pooled shape RMSE with hierarchical-bootstrap 95% confidence interval, and scene-wise phase lags after alignment.

Scene 2022081401 merits separate discussion because its phase lag reaches approximately −3.4 km while its geometric agreement after translation remains high (Fig. 9). This scene lies near Dongsha Atoll, where refraction, wave fission, and dissipation can restructure multi-crest packets (Fig. 7). Image inspection suggests that the leading soliton may have propagated beyond the representative-curve position, so the crestline near the evaluated longitude likely corresponds to the second wave in the packet. The 3.4 km offset is comparable to intra-packet soliton spacings observed in this corridor (e.g., Ramp et al., 2004), consistent with a crest-rank mismatch. The same scene also captures two wave groups near 117°E and 118.4°E; cloud cover obscures the eastern packet, and the representative curve supplies a continuous shape reference where satellite coverage is interrupted (Fig. 7a). This case illustrates both the utility of a climatological shape reference and the practical need for matching protocols that account for crest order within multi-crest packets.

https://doi.org/10.5194/egusphere-2026-4336
Preprint. Discussion started: 18 August 2026

Three points follow from the combined residual and phase analysis. First, the residual decomposition provides a clear operational separation between scene-level offset and phase-aligned shape mismatch, and the weak correlation between $|\delta|$ and the shape metrics (Fig. 10) shows that the two components carry distinct geometric information. Second, after removing scene-level offsets, the pooled shape error is $\mathrm{RMSE}_{\mathrm{shape}}$ = 1004 m (95% CI: 787–1220 m)—well below typical ISW crest-to-crest separations (5–20 km) and comparable to soliton half-widths reported in the northern South China Sea (Zheng et al., 2001; Song et al., 2021). Third, the scenes with elevated residuals (20150806, 20150815, and 2022081401) are each traceable to identifiable event-scale mechanisms—localized wavefront deformation or crest-rank mismatch—rather than to a curve-wide loss of geometric agreement. Together with the independent IOCAS/MODIS evaluation, these results show that the August monthly-climatological framework provides a kilometer-scale representation of the surface-expressed leading-crestline shape in the tested corridor. Beyond quantifying accuracy, this decomposition carries a physical implication. Consistent with the expectation set out in Section 2.1, event-scale currents, eddies, and source variability introduce both scene-level offsets and local shape deviations, and these appear in the evaluation as two distinguishable components; in the tested scenes, however, neither component obscures the large-scale common morphology captured by the month-specific representative curves. The crestline shape observed at the sea surface thus carries information about the propagation environment the wave has traversed, and the monthly representative curves capture the repeatable large-scale component of this shape—precisely the property that allows a monthly coefficient table, constructed without information specific to the evaluated event, to serve as a meaningful reference for observed crestlines.

3.4 Extension of the independent evaluation to additional calendar months

Under the monthly climatological framework, the workflow of Sections 2.4–2.5 was applied to the MITgcm-derived SSHG fields to construct representative leading-crestline curves and the corresponding coefficient tables for all 12 calendar months (Section 3.1). To evaluate these curves beyond the August demonstration, one independent satellite case was selected from each of May, June, and July: 18 May 2014, 6 June 2015, and 30 July 2014. Each observed crestline is compared exclusively with the representative curves of its own calendar month, using the crestline-to-curve metrics of Section 3.2 and the phase-aligned residual decomposition of Section 3.3. Fig. 13 provides the scene-level observational context for the three cases, and Fig. 14 reports the corresponding quantitative evaluations.

https://doi.org/10.5194/egusphere-2026-4336
Preprint. Discussion started: 18 August 2026

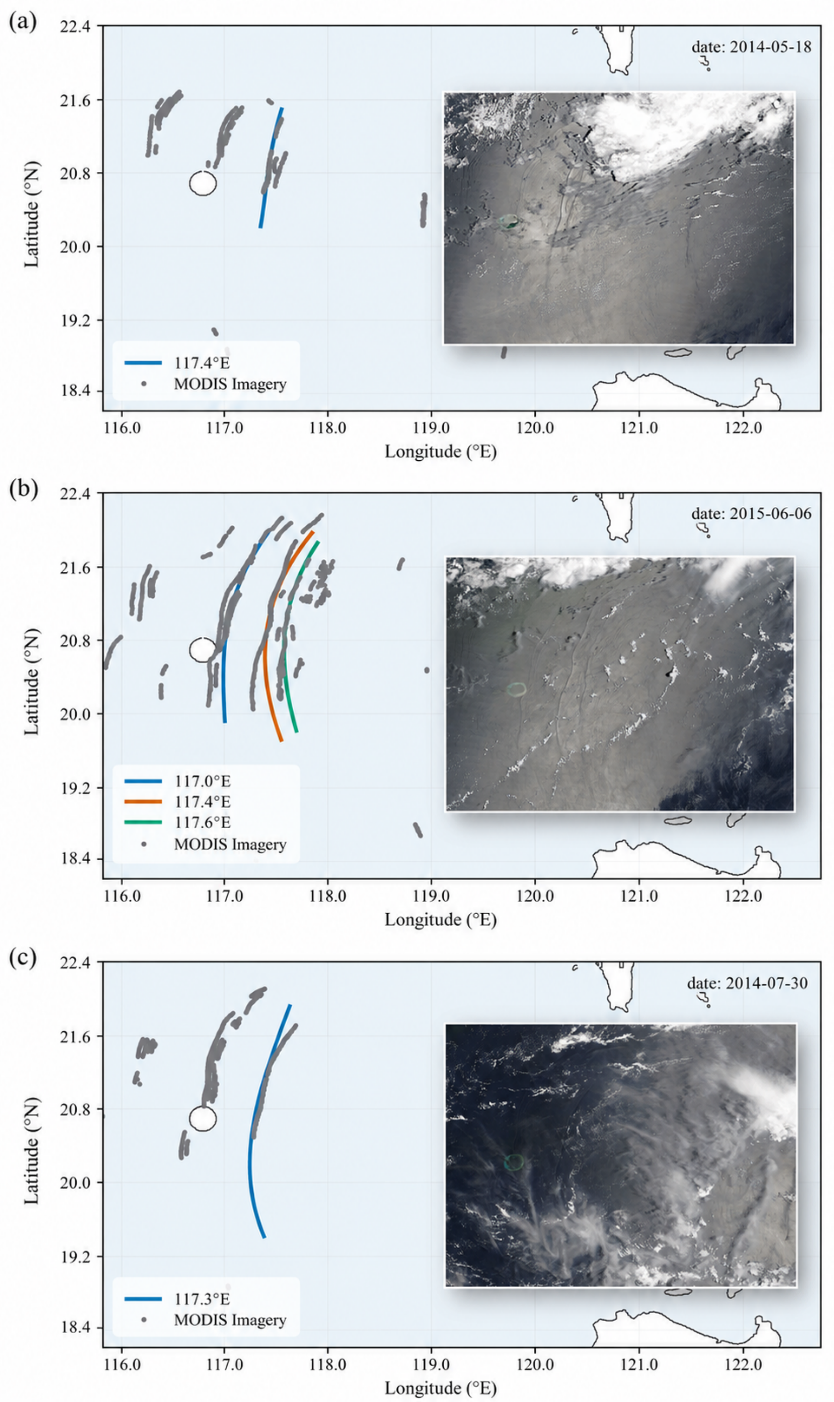

505 **Figure 13: Scene-level observational overview of the May, June, and July cases. Monthly representative leading-crestline curves are overlaid on the corresponding MODIS scenes for (a) 18 May 2014, (b) 6 June 2015, and (c) 30 July 2014. Gray signatures denote MODIS-extracted crestline observations, and colored curves denote the monthly representative curves. These panels provide the observational setting for the case-level results reported in Fig. 14.**

https://doi.org/10.5194/egusphere-2026-4336
Preprint. Discussion started: 18 August 2026

The results in Fig. 14a–c show that the month-specific representative curves retain the dominant large-scale crestline pattern in all three cases. For 18 May 2014, the comparison gives $N = 51$, $\mathrm{RMSE}_{\Delta\mathrm{Lon}} = 1354$ m, and $R^2 = 0.951$; for 6 June 2015, $N = 114$, $\mathrm{RMSE}_{\Delta\mathrm{Lon}} = 1247$ m, and $R^2 = 0.992$. The May and June cases therefore combine high R^2 values with absolute errors close to the August ensemble mean (1021 m), supporting the applicability of the month-specific representative curves beyond the August demonstration. For 30 July 2014, the comparison gives $N = 197$, $\mathrm{RMSE}_{\Delta\mathrm{Lon}} = 3247$ m, and $R^2 = 0.930$: the dominant crestline pattern is still captured, but more pronounced local departures from the representative curve raise the absolute error, analogous to the event-scale deformation identified for scene 20150806 in Section 3.3.

The phase-aligned shape residuals ΔE in Fig. 14d show the same case-to-case contrast. The May and June residual distributions are concentrated near zero, whereas the July distribution is broader with a more pronounced long tail, consistent with its larger $\mathrm{RMSE}_{\Delta\mathrm{Lon}}$ and with localized event-scale shape mismatch that persists after the scene-level offset is removed. These behaviors mirror the residual diagnostics of Section 3.3: the month-specific representative curves retain the dominant observed crestline pattern, while localized event-scale deformation appears as elevated residuals. Together with the August evaluation, these cases indicate that the monthly workflow—which constructs a representative-curve coefficient table for each calendar month—retains kilometer-scale agreement in each of the four months tested.

https://doi.org/10.5194/egusphere-2026-4336
Preprint. Discussion started: 18 August 2026

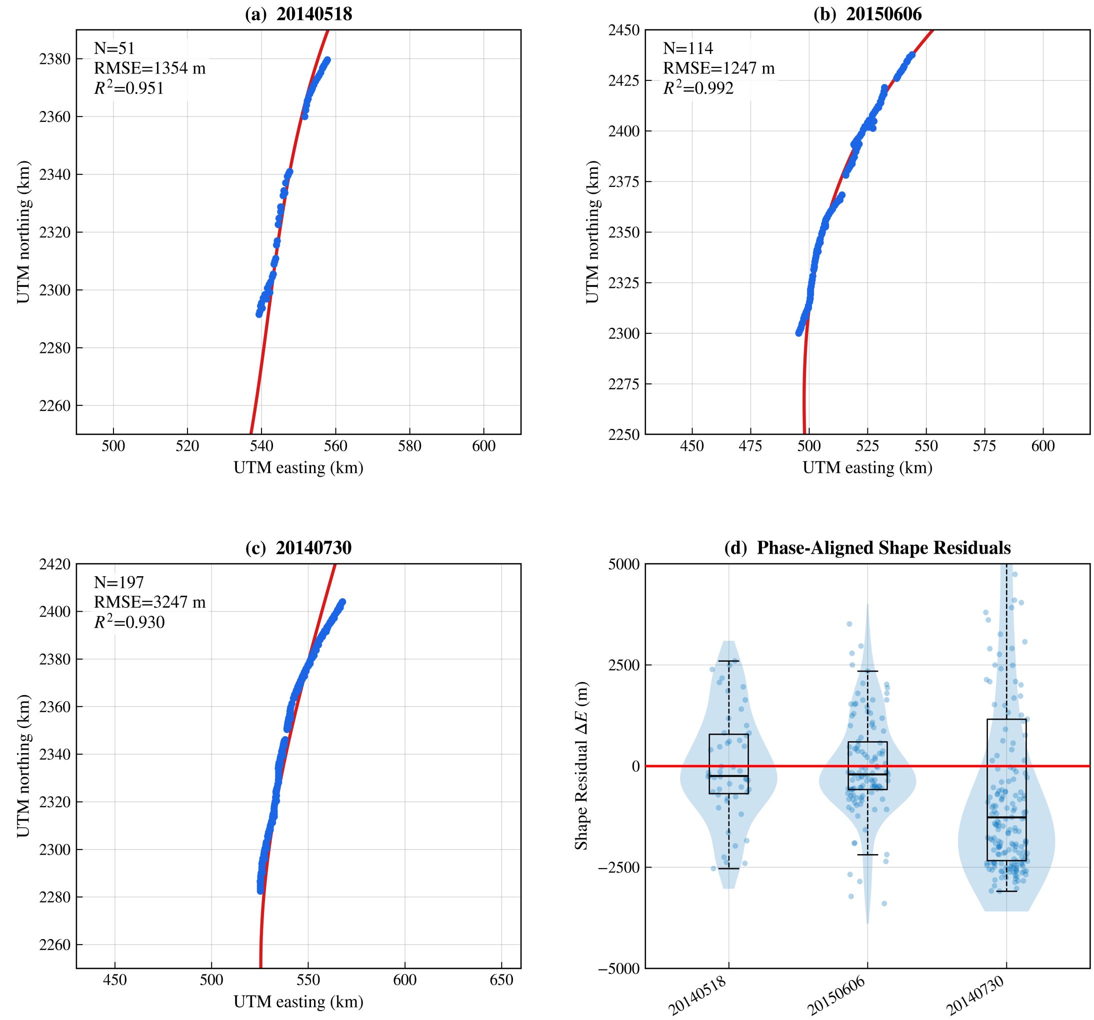

Figure 14: Independent case evaluations of month-specific representative curves for (a) 18 May 2014, (b) 6 June 2015, and (c) 30 July 2014. Red curves show the monthly representative crestline morphology, and blue points show the satellite-derived crest observations. Coordinates in (a–c) are shown in UTM Zone 50N, with easting and northing expressed in kilometers, as in Fig. 8. Each panel reports N, $\mathrm{RMSE}_{\Delta\mathrm{Lon}}$, and R^2. (d) Phase-aligned shape residuals ΔE (in meters) for the three cases: violin-box plots summarize the residual distributions after removing the scene-level offset, and the red line marks $\Delta E = 0$.

4 Conclusion

Predicting the morphology of surface-expressed leading ISW crestlines east of Dongsha Atoll is challenging because crestline shape is jointly controlled by background circulation, vertical stratification, bathymetric steering, and other dynamical processes whose combined effects are difficult to disentangle. The leading-crestline morphology parameterized in this study is more than a two-dimensional pattern extracted from sea-surface fields; it is grounded in the physics of internal-wave propagation. The SSHG source fields are generated by nonhydrostatic simulations that retain the two principal background

https://doi.org/10.5194/egusphere-2026-4336
Preprint. Discussion started: 18 August 2026

controls of the present framework—realistic bathymetry and WOA18 monthly stratification—so each extracted crestline is the sea-surface expression of a three-dimensional, stratification-conditioned propagation process: its position locates the surface signature of the leading wave; its local normal, combined with the known westward propagation in this corridor, indicates the local propagation direction; and its curvature reflects the accumulated effects of spatially differential propagation along the path, including refraction. The independent satellite evaluation supports the physical relevance and observational applicability of this representation: representative curves constructed only from monthly climatological conditions reproduce observed crestlines at kilometer scale in each of the calendar months tested, and the large-scale common morphology they describe remains identifiable in the presence of scene-level offsets and localized event-scale deformation. The shape of the surface leading crestline therefore carries physically meaningful information about the propagation conditions in the underlying stratified ocean, and it is this property that allows the monthly coefficient tables, which contain no information specific to the evaluated event, to serve as a physically grounded reference for observed crestlines. Based on WOA18 monthly stratification, this study adopted a monthly climatological-mean framework and analyzed SSHG fields derived from nonhydrostatic MITgcm simulations (Gong et al., 2023, 2025) to investigate the common propagation morphology of surface-expressed leading ISW crestlines in the east-of-Dongsha segment of the Luzon Strait–Dongsha corridor. The representative curves were constructed from MITgcm-derived SSHG fields, whereas IOCAS/MODIS satellite-derived crestlines were reserved for independent evaluation.

Under monthly-mean conditions, leading crestlines within the same calendar month and crossing-longitude bin cluster around a repeatable, location-dependent common morphology that can be compactly represented by a cubic polynomial, $\mathrm{Lon} = C_0\mathrm{Lat}^3 + C_1\mathrm{Lat}^2 + C_2\mathrm{Lat} + C_3$. This consistency indicates that the month-specific waveguide, governed primarily by fixed bathymetry and the seasonally varying pycnocline structure, constrains the large-scale bending of surface-expressed leading crestlines. For the August demonstration, nine independent satellite-derived crestline objects from 2014, 2015, and 2022 yield a mean R^2 of 0.870, RMSE of 1021 m, and KGE of 0.789; after phase alignment, the pooled morphology error is 1.004 km, with a 95% confidence interval of 0.787–1.220 km. The selected May, June, and July cases further show that the corresponding month-specific representative curves retain the broad surface-crestline pattern outside the August demonstration, with case-dependent local departures. These results show that, at climatological scales, the surface-expressed leading-crestline morphology can be represented through direct polynomial evaluation of monthly representative curves, providing a compact and interpretable reference for regional ISW crestline mapping, rapid forecasting of crestline position and shape.

The present formulation also points to several directions for further development. Higher-temporal-resolution stratification, background currents, and mesoscale conditions can be incorporated to better represent event-scale offsets and local residual deformations. The more complex region at and west of Dongsha Atoll, where diffraction, refraction, shoaling, fission, and multi-crest interactions become prominent, motivates a separate extension of the representative-curve framework. Finally, this study focuses on the horizontal surface expression of the leading crestline, namely its position, orientation, and curvature. Event-specific waveform, amplitude, vertical displacement, and other subsurface structures require a separate three-

https://doi.org/10.5194/egusphere-2026-4336
Preprint. Discussion started: 18 August 2026

dimensional treatment. Future work will extend the same parameterization and independent-evaluation strategy to broader month-by-month satellite evaluations, more complex propagation regimes around Dongsha Atoll, and coupled surface-subsurface descriptions of ISW evolution.

Data availability

The satellite-derived internal-wave crestline observations used for validation in this study were obtained from the 22-year internal wave dataset for the northern South China Sea developed by Zhang and Li (2024), which is publicly available at https://doi.org/10.12157/IOCAS.20240409.001.

Author contributions

YY contributed to conceptualization, formal analysis, methodology, validation, writing of the original draft, and review and editing of the manuscript. YG contributed to resources, software, supervision, and review and editing of the manuscript. XW contributed to funding acquisition, methodology, project administration, resources, supervision, and review and editing of the manuscript.

Competing interests

The authors declare that they have no conflict of interest.

Acknowledgements

The authors would like to express their gratitude to the Oceanographic Data Center, Chinese Academy of Sciences (CODC, https://www.casodc.com/) for providing the essential data for this study. Special thanks are extended to Xudong Zhang for his generosity in sharing the database and for his guidance of the study.

Financial support

This research has been supported by the National Natural Science Foundation of China (grant nos. 11972352, 52394254, and 12132018).

https://doi.org/10.5194/egusphere-2026-4336
Preprint. Discussion started: 18 August 2026

References

Alford, M. H., Lien, R.-C., Simmons, H., Klymak, J. M., Ramp, S. R., Yang, Y. J., Tang, D., and Chang, M.-H.: Speed and evolution of nonlinear internal waves transiting the South China Sea, J. Phys. Oceanogr., 40, 1338–1355, https://doi.org/10.1175/2010JPO4388.1, 2010.

Alford, M. H., Peacock, T., MacKinnon, J. A., Nash, J. D., Buijsman, M. C., Centurioni, L. R., Chao, S.-Y., Chang, M.-H., Farmer, D. M., Fringer, O. B., Fu, K.-H., Gallacher, P. C., Graber, H. C., Helfrich, K. R., Jachec, S. M., Jackson, C. R., Klymak, J. M., Ko, D. S., Jan, S., Johnston, T. M. S., Legg, S., Lee, I. H., Lien, R.-C., Mercier, M. J., Moum, J. N., Musgrave, R., Park, J.-H., Pickering, A. I., Pinkel, R., Rainville, L., Ramp, S. R., Rudnick, D. L., Sarkar, S., Scotti, A., Simmons, H. L., St Laurent, L. C., Venayagamoorthy, S. K., Wang, Y.-H., Wang, J., Yang, Y. J., Paluszkiewicz, T., and Tang, T.-Y.: The formation and fate of internal waves in the South China Sea, Nature, 521, 65–69, https://doi.org/10.1038/nature14399, 2015.

Apel, J. R., Holbrook, J. R., Liu, A. K., and Tsai, J. J.: The Sulu Sea internal soliton experiment, J. Phys. Oceanogr., 15, 1625–1651, https://doi.org/10.1175/1520-0485(1985)015%3C1625:TSSISE%3E2.0.CO;2, 1985.

Bai, X., Liu, Z., Li, X., and Hu, J.: Generation sites of internal solitary waves in the southern Taiwan Strait revealed by MODIS true-colour image observations, Int. J. Remote Sens., 35, 4086–4098, https://doi.org/10.1080/01431161.2014.916453, 2014.

Bai, X., Li, X., Lamb, K. G., and Hu, J.: Internal solitary wave reflection near Dongsha Atoll, the South China Sea, J. Geophys. Res.-Oceans, 122, 7978–7991, https://doi.org/10.1002/2017JC012880, 2017.

Cai, S., Long, X., and Gan, Z.: A numerical study of the generation and propagation of internal solitary waves in the Luzon Strait, Oceanol. Acta, 25, 51–60, https://doi.org/10.1016/S0399-1784(02)01181-7, 2002.

Cai, S., Xie, J., and He, J.: An overview of internal solitary waves in the South China Sea, Surv. Geophys., 33, 927–943, https://doi.org/10.1007/S10712-012-9176-0, 2012.

Canny, J.: A computational approach to edge detection, IEEE Trans. Pattern Anal. Mach. Intell., 8, 679–698, https://doi.org/10.1109/TPAMI.1986.4767851, 1986.

Chen, C., Beardsley, R. C., and Cowles, G.: An unstructured grid, finite-volume coastal ocean model (FVCOM) system, Oceanography, 19, 78–89, https://doi.org/10.5670/oceanog.2006.92, 2006.

Chen, L., Zheng, Q., Xiong, X., Yuan, Y., Xie, H., Guo, Y., Yu, L., and Yun, S.: Dynamic and statistical features of internal solitary waves on the continental slope in the northern South China Sea derived from mooring observations, J. Geophys. Res.-Oceans, 124, 4078–4097, https://doi.org/10.1029/2018JC014843, 2019.

Cheng, Y.-H., Chang, M.-H., Yang, Y. J., Jan, S., Ramp, S. R., Davis, K. A., and Reeder, D. B.: Insights into internal solitary waves east of Dongsha Atoll from integrating geostationary satellite and mooring observations, J. Geophys. Res.-Oceans, 129, e2024JC021109, https://doi.org/10.1029/2024JC021109, 2024.

Cui, Z., Liang, C., Lin, F., Chen, S., Ding, T., Zhou, B., Jin, W., and Yang, W.: Construction of a wavefront model for internal solitary waves and its application in the northern South China Sea, Ocean Model., 189, 102366, https://doi.org/10.1016/j.ocemod.2024.102366, 2024.

https://doi.org/10.5194/egusphere-2026-4336
Preprint. Discussion started: 18 August 2026

Dang, X., Sui, Y., Tang, D., Wang, J., and Chen, S.: Himawari sea surface temperature data reveal regular internal wave activity producing cooling in the northern South China Sea, Front. Mar. Sci., 12, 1523449, https://doi.org/10.3389/fmars.2025.1523449, 2025.

Ester, M., Kriegel, H.-P., Sander, J., and Xu, X.: A density-based algorithm for discovering clusters in large spatial databases with noise, in: Proceedings of the Second International Conference on Knowledge Discovery and Data Mining (KDD'96), 226–231, 1996.

Fringer, O. B., Gerritsen, M., and Street, R. L.: An unstructured-grid, finite-volume, nonhydrostatic, parallel coastal-ocean simulator: SUNTANS, Ocean Model., 14, 139–173, https://doi.org/10.1016/j.ocemod.2006.05.006, 2006.

Fu, L.-L. and Holt, B.: Seasat views oceans and sea ice with synthetic-aperture radar, Jet Propulsion Laboratory, Pasadena, California, USA, JPL Publication 81-120, 1982.

Gong, Y., Chen, X., Xu, J., Xie, J., Chen, Z., He, Y., and Cai, S.: An internal solitary wave forecasting model in the northern South China Sea (ISWFM-NSCS), Geosci. Model Dev., 16, 2851–2871, https://doi.org/10.5194/gmd-16-2851-2023, 2023.

Gong, Y., Chen, X., Xu, J., Chen, Z., He, Q., Zhao, R., Zhu, X.-H., and Cai, S.: ISWNM-NSCS v2.0: Advancing the internal solitary wave numerical model with background currents and horizontally inhomogeneous stratifications, Geosci. Model Dev., 18, 5413–5433, https://doi.org/10.5194/gmd-18-5413-2025, 2025.

Guo, C. and Chen, X.: A review of internal solitary wave dynamics in the northern South China Sea, Prog. Oceanogr., 121, 7–23, https://doi.org/10.1016/j.pocean.2013.04.002, 2014.

Huang, H., Song, P., Qiu, S., Guo, J., and Chen, X.: A nonhydrostatic oceanic regional model, ORCTM v1, for internal solitary wave simulation, Geosci. Model Dev., 16, 109–133, https://doi.org/10.5194/gmd-16-109-2023, 2023.

Huang, H., Qiu, S., Zeng, Z., Song, P., Guo, J., and Chen, X.: Modulation of internal solitary waves by one mesoscale eddy pair west of the Luzon Strait, J. Phys. Oceanogr., 54, 2133–2152, https://doi.org/10.1175/JPO-D-23-0244.1, 2024.

Jia, T., Liang, J. J., Li, X.-M., and Sha, J.: SAR observation and numerical simulation of internal solitary wave refraction and reconnection behind Dongsha Atoll, J. Geophys. Res.-Oceans, 123, 74–89, https://doi.org/10.1002/2017JC013389, 2018.

Jiang, S., Dai, D., Wang, D., Wang, S., Li, Y., Guo, J., and Qiao, F.: Inferring diapycnal mixing using the internal wave continuum from the high-resolution ocean model, Ocean Model., 195, 102525, https://doi.org/10.1016/j.ocemod.2025.102525, 2025.

Kurekin, A. A., Land, P. E., and Miller, P. I.: Internal waves at the UK continental shelf: Automatic mapping using the ENVISAT ASAR sensor, Remote Sens., 12, 2476, https://doi.org/10.3390/rs12152476, 2020.

Li, J.: Billow under the sea surface: Internal waves in the ocean, Mechanics in Engineering, 27, 1–6, https://doi.org/10.6052/1000-0992-2005-107, 2005.

Li, Q., Wang, B., Chen, X., Chen, X. E., and Park, J.-H.: Variability of nonlinear internal waves in the South China Sea affected by the Kuroshio and mesoscale eddies, J. Geophys. Res.-Oceans, 121, 2098–2118, https://doi.org/10.1002/2015JC011134, 2016.

https://doi.org/10.5194/egusphere-2026-4336
Preprint. Discussion started: 18 August 2026

Li, X., Jackson, C. R., and Pichel, W. G.: Internal solitary wave refraction at Dongsha Atoll, South China Sea, Geophys. Res. Lett., 40, 3128–3132, https://doi.org/10.1002/grl.50614, 2013.

Liang, J., Li, X.-M., Sha, J., Jia, T., and Ren, Y.: The lifecycle of nonlinear internal waves in the northwestern South China Sea, J. Phys. Oceanogr., 49, 2133–2145, https://doi.org/10.1175/JPO-D-18-0231.1, 2019.

Liu, A. K. and Hsu, M. K.: Internal wave study in the South China Sea using synthetic aperture radar (SAR), Int. J. Remote Sens., 25, 1261–1264, https://doi.org/10.1080/01431160310001592148, 2004.

Locarnini, R. A., Mishonov, A. V., Baranova, O. K., Boyer, T. P., Zweng, M. M., Garcia, H. E., Reagan, J. R., Seidov, D., Weathers, K. W., Paver, C. R., and Smolyar, I. V.: World Ocean Atlas 2018, Volume 1: Temperature, edited by: Mishonov, A., NOAA Atlas NESDIS 81, 52 pp., https://doi.org/10.25923/e5rn-9711, 2019.

Marshall, J., Adcroft, A., Hill, C., Perelman, L., and Heisey, C.: A finite-volume, incompressible Navier–Stokes model for studies of the ocean on parallel computers, J. Geophys. Res.-Oceans, 102, 5753–5766, https://doi.org/10.1029/96JC02775, 1997.

Meng, L., Song, H., Guan, Y., Yang, S., Zhang, K., and Liu, M.: Energy transfer from internal solitary waves to turbulence via high-frequency internal waves: Seismic observations in the northern South China Sea, Nonlin. Processes Geophys., 31, 477–495, https://doi.org/10.5194/npg-31-477-2024, 2024.

Min, W., Li, Q., Xu, Z., Wang, Y., Li, D., Zhang, P., Robertson, R., and Yin, B.: High-resolution, non-hydrostatic simulation of internal tides and solitary waves in the southern East China Sea, Ocean Model., 181, 102141, https://doi.org/10.1016/j.ocemod.2022.102141, 2023.

Park, J.-H. and Farmer, D.: Effects of Kuroshio intrusions on nonlinear internal waves in the South China Sea during winter, J. Geophys. Res.-Oceans, 118, 7081–7094, https://doi.org/10.1002/2013JC008983, 2013.

Ramp, S. R., Tang, T.-Y., Duda, T. F., Lynch, J. F., Liu, A. K., Chiu, C.-S., Bahr, F. L., Kim, H.-R., and Yang, Y.-J.: Internal solitons in the northeastern South China Sea, Part I: Sources and deep water propagation, IEEE J. Oceanic Eng., 29, 1157–1181, https://doi.org/10.1109/JOE.2004.840839, 2004.

Ramp, S. R., Yang, Y. J., Chiu, C.-S., Reeder, D. B., and Bahr, F. L.: Observations of shoaling internal wave transformation over a gentle slope in the South China Sea, Nonlin. Processes Geophys., 29, 279–299, https://doi.org/10.5194/npg-29-279-2022, 2022.

Saravanan, V., Berman, G. J., and Sober, S. J.: Application of the hierarchical bootstrap to multi-level data in neuroscience, arXiv [preprint], arXiv:2007.07797, https://doi.org/10.48550/arXiv.2007.07797, 2020.

Simmons, H., Chang, M.-H., Chang, Y.-T., Chao, S.-Y., Fringer, O. B., Jackson, C. R., and Ko, D. S.: Modeling and prediction of internal waves in the South China Sea, Oceanography, 24, 88–99, https://doi.org/10.5670/oceanog.2011.97, 2011.

Sinnett, G., Ramp, S. R., Yang, Y. J., Chang, M.-H., Jan, S., and Davis, K. A.: Large-amplitude internal wave transformation into shallow water, J. Phys. Oceanogr., 52, 2539–2554, https://doi.org/10.1175/JPO-D-21-0273.1, 2022.

Song, H., Gong, Y., Yang, S., and Guan, Y.: Observations of internal structure changes in shoaling internal solitary waves based on seismic oceanography method, Front. Mar. Sci., 8, 733959, https://doi.org/10.3389/fmars.2021.733959, 2021.

https://doi.org/10.5194/egusphere-2026-4336
Preprint. Discussion started: 18 August 2026

Xie, J., Fang, W., He, Y., Chen, Z., Liu, G., Gong, Y., and Cai, S.: Variation of internal solitary wave propagation induced by the typical oceanic circulation patterns in the northern South China Sea deep basin, Geophys. Res. Lett., 48, e2021GL093969, https://doi.org/10.1029/2021GL093969, 2021.

Xun, H., Zhou, C., Xiao, X., Guan, S., Huang, X., Qu, T., Zhao, W., and Tian, J.: Variability of turbulent mixing observed by high-resolution acoustic Doppler current profilers in the deep South China Sea, Front. Mar. Sci., 12, 1643170, https://doi.org/10.3389/fmars.2025.1643170, 2025.

Zeng, K., Lyu, R., Li, H., Suo, R., Du, T., and He, M.: Studying the internal wave generation mechanism in the northern South China Sea using numerical simulation, synthetic aperture radar, and in situ measurements, Remote Sens., 16, 1440, https://doi.org/10.3390/rs16081440, 2024.

Zeng, Z., Chen, X., Yuan, C., and Song, J.: A case study of wave–wave interaction south to Dongsha Island in the South China Sea, Remote Sens., 16, 337, https://doi.org/10.3390/rs16020337, 2024.

Zhang, M., Wang, J., Chen, X., Mei, Y., and Zhang, X.: An experimental study on the characteristic pattern of internal solitary waves in optical remote-sensing images, Int. J. Remote Sens., 40, 7017–7032, https://doi.org/10.1080/01431161.2019.1597308, 2019.

Zhang, S., Li, X., and Zhang, X.: Internal wave signature extraction from SAR and optical satellite imagery based on deep learning, IEEE Trans. Geosci. Remote Sens., 61, 1–16, https://doi.org/10.1109/TGRS.2023.3258189, 2023.

Zhang, X. and Li, X.: Constructing a 22-year internal wave dataset for the northern South China Sea: Spatiotemporal analysis using MODIS imagery and deep learning, Earth Syst. Sci. Data, 16, 5131–5144, https://doi.org/10.5194/essd-16-5131-2024, 2024.

Zhang, X., Li, X., and Zheng, Q.: A machine-learning model for forecasting internal wave propagation in the Andaman Sea, IEEE J. Sel. Top. Appl. Earth Obs. Remote Sens., 14, 3095–3106, https://doi.org/10.1109/JSTARS.2021.3063529, 2021.

Zhao, Z. and Alford, M. H.: Source and propagation of internal solitary waves in the northeastern South China Sea, J. Geophys. Res.-Oceans, 111, C11012, https://doi.org/10.1029/2006JC003644, 2006.

Zheng, Q., Yuan, Y., Klemas, V., and Yan, X.-H.: Theoretical expression for an ocean internal soliton synthetic aperture radar image and determination of the soliton characteristic half width, J. Geophys. Res.-Oceans, 106, 31415–31423, https://doi.org/10.1029/2000JC000726, 2001.

Zweng, M. M., Reagan, J. R., Seidov, D., Boyer, T. P., Locarnini, R. A., Garcia, H. E., Mishonov, A. V., Baranova, O. K., Weathers, K. W., Paver, C. R., and Smolyar, I. V.: World Ocean Atlas 2018, Volume 2: Salinity, edited by: Mishonov, A., NOAA Atlas NESDIS 82, 50 pp., https://doi.org/10.25923/9pgv-1224, 2019.